NEW ASTROPHYSICAL PROBES OF DARK MATTER

by

Mei-Yu Wang

B.S. in Physics, National Taiwan Normal University, 2004

M.S. in Physics, University of Pittsburgh, 2007

Submitted to the Graduate Faculty of

the Kenneth P. Dietrich School of Arts & Sciences in partial fulfillment

of the requirements for the degree of

Doctor of Philosophy

University of Pittsburgh

2012

UNIVERSITY OF PITTSBURGH

DEPARTMENT OF PHYSICS & ASTRONOMY

This dissertation was presented

by

Mei-Yu Wang

It was defended on

November 27th

and approved by

Andrew Zentner, Department of Physics & Astronomy, University of Pittsburgh

Arthur Kosowsky, Department of Physics & Astronomy, University of Pittsburgh

Jeffery Newman, Department of Physics & Astronomy, University of Pittsburgh

Vladimir Savinov, Department of Physics & Astronomy, University of Pittsburgh

Tiziana Di Matteo, Department of Physics, Carnegie Mellon University

Dissertation Director: Andrew Zentner, Department of Physics & Astronomy, University of Pittsburgh

NEW ASTROPHYSICAL PROBES OF DARK MATTER

Mei-Yu Wang, PhD

University of Pittsburgh, 2012

In my thesis, I present four studies to explore astrophysical methods for understanding dark matter properties. To understand the nature of dark matter, I explore a few unstable dark matter models that are invoked as ways to address apparent discrepancies between the predictions of standard cold dark matter and observations of small-scale galactic structure. My studies are aimed at developing independent large-scale constraints on these models. One of the model is a decaying dark matter model such that one dark matter particle decays into two relativistic non-interacting particles. In the second model, a dark matter particle decays into a less massive, stable dark matter particle with a recoil kick velocity V_k and a relativistic non-interacting particle. I consider two types of experiments: one is weak lensing cosmic shear with future or forthcoming surveys like Dark Energy Survey (DES) and Large Synoptic Survey Telescope (LSST); the other one is Lyman-α forest spectrum, which has contemporary data from Sloan Digital Sky Survey (SDSS) and other observations. I found that large-scale structure growth is sensitive to the change of dark matter properties due to these decay processes, and they can provide competitive constraints comparing to other existing limits. On small scale, the gravitational interplay of baryon and dark matter can affect the clustering of dark matter. I examine adiabatic contraction (AC) models what are traditionally used to parametrize the dark matter response to the cooling of baryons by investigating a suite of numerical simulations. We found that the errors in AC reconstructions are correlated with baryonic physics and certain halo properties. Our results indicate that existing AC models need significant calibration in order to predicting realistic matter distribution.

TABLE OF CONTENTS

LIST OF TABLES

LIST OF FIGURES

1.0 INTRODUCTION

Many and various astronomical observations indicate that $\sim 5/6$ of the mass density of the Universe is non-baryonic *dark matter* (reviews include [1, 2, 3]). The simplest model of so-called *cold* dark matter (CDM) can be successfully applied to interpret an enormous amount of observational data, particularly those characterizing the large-scale ($\gtrsim$ a few Mpc) structure of the Universe and the gross properties of galaxies. In particular, the CDM model is consistent with the cosmic microwave background (CMB) anisotropy spectrum measured by the Wilkinson Microwave Anisotropy Probe (WMAP) and observations of the large-scale ($k \lesssim 0.1$h/Mpc) galaxy clustering spectrum measured by the Sloan Digital Sky Survey (SDSS) [4]. Despite of the success of CDM model on large scales, the nature of dark matter is still unknown.

On smaller scales, the situation is murkier. Several observations indicate possible discrepancies between CDM theory and observations on smaller scales. Among these are the well-known *missing satellites problem* [5, 6] and the steep rotation curves of low-surface brightness galaxies [7, 8, 9]. Also, a recent analysis by [10] puts forward an additional challenge to the CDM model. The authors used simulated MW-like haloes in a CDM cosmology to show that massive subhalos of MW-like haloes seem to be too dense to host the bright MW dSphs. On the theoretical side, it is necessary to model highly nonlinear phenomena to predict the properties of galaxies and the dark matter halos in which they reside. Nevertheless, these potential shortcomings of CDM may point toward novel properties of dark matter and many alternatives to CDM have been considered, including *warm* dark matter (WDM) [11, 12, 13, 14, 15], self-interacting dark matter (SIDM) [16], and dark matter that decays with long lifetime [17, 18, 19, 20, 21, 22]. These different models are invoked to solve the small scale problem, and yet recently studies have shown that they solve the different

small scale problems in different levels (for example, [23, 24, 25, 26]). As the observational data and theoretical prediction accuracy improves, we will soon have the ability to determine which one will provide the best solution. So many people are now putting efforts to explore these models in details.

Although these alternative dark matter models are aimed to solve the small scale problem, so far some of the most robust constraints come from large-scale observations. In our work we investigate two classes of decaying dark matter and their impact on large-scale structure growth. One is a benchmark decaying dark matter model such that one dark matter particle decays into two relativistic non-interacting particles [27]. Current best constraints on this model come from WMAP experiment [28]. The sensitivity of this observable comes from the change of universe expansion history and late integrated Sachs-Wolfe (LISW) effect due to increment in relativistic energy budget. In our work [21], we explore the effect of decaying dark matter on large-scale matter fluctuation growth by solving the full sets of perturbation equations using CMBFAST. We also discuss the possible effect on dark matter halo density profiles to account for the modification in nonlinear scale. In our following work [22], we examine a another class of decaying dark matter model which has been considered in a number of recent studies [17, 18, 19, 20, 29, 30, 31]. In such models, a dark matter particle of mass M decays into a less massive daughter particle of mass m = (1 -f)M and a significantly lighter, relativistic particle, with a lifetime on the order of the age of the Universe. The mass difference will introduce an excess kick velocity $V_k \sim fc$ to the stable daughter dark matter particles relative to their parent particles, where c is the speed of light. The kick velocity at decay imparts upon the stable daughter particles the ability to smooth gravitational potential perturbations on scales smaller than the classic free-streaming scale. This behavior is similar to the cosmological influence of massive neutrinos or WDM. This free-streaming effect of decaying dark matter has been explored by [31]. In our work, we investigate this effect on cosmological perturbation evolution by solving perturbation equations in the non-relativisitc kick velocity limits and look in details of their effects on structure growth.

To consider constraints from large-scale structure growth, it was noted that the observations of power on the smallest linear scales in the Lyman-α forest may provide particularly

stringent constraints. This technique is found to provide particularly stringent constraints on WDM [32], one of the most motivated alternative dark matter model. The current Lyman-α forest data can probe linear fluctuation up to a few Mpc around redshift z$\sim$2-4 [33, 34, 35]. It has been point out recently [24, 25] that the allowed WDM mass from Lyman-α analysis [36, 37]is not sufficient to explain the observed core size in dwarf galaxies. The tension between large-scale and small scale observation in WDM may be able to find solutions in baryonic feedback [38, 24, 39] or novel properties of WDM [40]. Following the results of recent WDM study, it will be interested to see how other alternative dark matter models will behave in these checks and understand whether they can provide a more reasonable solution to this small and large-scale tension that can not be solved by WDM. We are thus motivated to investigate the effect of decaying dark matter on Lyman-α forest observation. In our work, we choose to look at the decay model that generate a kick to the daughter particle [18, 19, 29]. The decay process also suppresses structure growth below the free-streaming scale like WDM, but the free-streaming scale increases with time as the decaying happens, which is opposite to WDM. We will utilize both the Lyman-α-forest-derived matter power spectrum data set[33, 34, 41] and SDSS Lyman-α forest flux power spectrum [35]. The approaches to analyze these two types of data are different, and the SDSS data set requires running numerical simulations to calibrate it due to the small systematics error. We will describe the details of the data and our approaches later in the methodology section.

Along with the Lyman-α forest method, weak lensing surveys can be used to probe further clustering properties of dark matter particles on sub-galactic scales, as the next generation of these surveys (such as e.g. LSST, WFIRST, Euclid) will be able to measure the matter power spectrum at scales down to 1 - 10 h/Mpc with a few percent accuracy. Recently [42] argued that future weak lensing survey can provide competitive constraining power for WDM properties with the existing Lyman-α limits. However, the main challenge for the weak lensing is to properly calibrate the nonlinear scale of matter power spectrum. The effect of alternative dark matter model on nonlinear structure evolution can be calibrated numerically [43, 44] and theoretically [45]. The effect from baryonic physics is also important at the nonlinear scale. However, there are still debates about how baryonic physics affect matter distribution. It is generally believed that as baryons cool and fall toward the center of a dark

matter halo, their condensation pulls the host material along, increasing the central density of the halo [46, 47, 48]. These effect can be modeled by a modified halo concentration-mass relation and it will boost the weak lensing signal due to the increment in nonlinear power [49]. However, several recent studies that investigate the effect of baryonic feedback had found that including different baryonic processes may have different impact on matter distribution. It is possible to produce suppression of matter clustering through baryonic feedback [50, 51]. Thus it might be challenging to disentangle the effect from dark matter properties and baryon physics in the modification of nonlinear matter power spectrum. Before we can come up with a realistic way to model baryonic process, the power of future weak lensing measurement should be quoted with caution when nonlinear scale is included. Nevertheless, we show in our work that, even if we restrict to linear scale, forthcoming or future weak lensing experiment can still provide some interesting constraints on some unstable dark matter models.

Baryons interact with the dark matter gravitationally, so it is necessary to determine how baryonic processes alter the distribution of dark matter in the Universe. It is known that if the baryonic gravitational potential changes slowly, the corresponding dark matter distribution can be modeled by adiabatic contraction (AC) process [46, 47, 48]. However, this approach has been shown to have about 10-20 % difference in matter distribution prediction in numerical simulation tests that have been performes. Despite the inadequacies of theory, the process of adiabatic contraction has long been considered a part of standard galaxy formation lore and has been used extensively in the mass modelling of galaxies and clusters. AC models have also been used to study the origin of the Tully-Fisher relation for spiral galaxies [52, 53, 54], the expected γ-ray signal from secondary dark matter annihilation in the centers of galaxies [55, 56, 57, 58, 59], strong lensing [60, 61], and calibrations of the initial mass function [62]. Although adiabatic contraction provides a simple scheme for predicting dark matter distributions in the context of baryonic co-evolution, without the expensive need for fully hydrodynamical computations, the modelling of AC theory has become a source of uncertainty itself and must be carefully checked against the various input physics given to cosmological simulations. The problems arising in numerical simulation tests are likely due to the fact that the baryon potential change is too rapid to obey an adiabatic process. Not until recently the implementation of AGN in a wide range of numerical simulations, all simulations

suffered from the "overcooling problem." Baryons cool too rapidly, coalesce at the centers of halos, and form stars at a rate such that most simulations predict significantly greater amounts of stars than there are in observed galaxies. Adiabatic contraction models have been found to overestimate the actual dark matter distribution [47]. It is generally believed that including AGN feedback can prevent the overcooling of the baryonic component by ejecting large quantities of gas at high redshift, when the supermassive black holes were growing rapidly [63, 64]. Some studies found that in such strong feedback systems adiabatic contraction models can underestimate matter density distributions [65]. In our work, we show that with moderate AGN feedback, the adiabaticity of the system can be restored and thus the AC model prediction accuracy is improved. We also look for correlations between AC model behaviors and halo properties such that it can be linked to the effect of baryon physics to the environment. We will discuss the results and limits due to resolution issues in the conclusion section.

In this thesis, I present the results of three studies and one work on progress. The first two of these explore the effects of unstable dark matter on large-scale structures. In §2.1, I begin with the simple model of dark matter particles decay into purely relativistic species, then I also consider another class of model that dark matter particles decay into a massive daughter particle that is stable and had gained excess kick velocity during the decay process. The details of modified perturbation equations are described in §2.1.1 which are related to the evolution of linear structure growth. In §2.1.2 I use analytical methods to explore the impacts on dark matter halo. In these studies, I compute the effects of unstable dark matter on lensing power spectrum observables. I then estimate the precision of these observables to be measured with forthcoming data and the resulting constraints that can be placed on unstable dark matter models. The methods of weak lensing forecasting is described in §2.2. I present the results in §3.1 and conclusions in §4.

In §2.3, I move to contemporary constraints. The contemporary constraints that are least subject to specific assumptions about nonlinear effects are likely to come from the Lyman-α forest. This is because the Lyman-α forest is observed at high-redshift, when structure on relevant scales was more securely in the linear regime. Nevertheless, current and future data are sufficiently precise that numerical simulations are necessary to address this issue.

I will shortly explain the data that I adopt in my analysis in §2.3.1. I will also describe my simulation program in §2.3.2 to calibrate the effects from various model parameters and present my preliminary constraints on unstable dark matter from the Lyman-α forest in §3.2.

Finally, in §2.4, I will describe halo contraction in the presence of baryons. In this study I compared halo properties and test adiabatic contraction models in a suite of simulations that are implemented with different baryonic process. I will shortly describe some of the simulation features in §2.4. The details of the simulations are described in [66]. A few adiabatic contraction models have been proposed, and I will illustrate in §2.4.2 how I tested them in simulations. I will present my findings of how adiabatic contraction model predictions behave with baryon and halo properties in §3.3 and conclusions in §4.

2.0 METHODOLOGY

2.1 EFFECT OF DECAYING DARK MATTER MODELS ON STRUCTURE GROWTH

2.1.1 Linear perturbation evolution in decaying dark matter models

For the first unstable dark matter model, we explore a restricted set of models in which a massive parent dark matter particle decays into a significantly lighter pair of daughter particles. For the sake of specificity, we adopt a decaying dark matter (DDM) scenario in which massive majorana parent particles decay into relativistic daughter (RD) particles via two-body decay and use this scenario to benchmark observational constraints. In such a scenario, the lifetime of the unstable dark matter particle lifetime (Γ^{-1}) is the only non-standard free parameter. Here Γ is the decay rate and it is equal to inverse of the lifetime.

The distribution functions of DDM ($f_{\rm DDM}$) and RD ($f_{\rm RD}$) evolve according to the coupled Einstein-Boltzmann equations. In particular (e.g., [67, 27]),

$$\frac{df_{\rm DDM}}{d\tau} = -\frac{a^2 m_{\rm DDM}\Gamma}{\epsilon_{\rm DDM}} f_{\rm DDM} \simeq -a\Gamma f_{\rm DDM} \tag{2.1}$$

$$\frac{df_{\rm RD}}{d\tau} = \frac{a^2 m_{\rm DDM}\Gamma}{\epsilon_{\rm DDM}} f_{\rm DDM} \simeq a\Gamma f_{\rm DDM}, \tag{2.2}$$

where τ is the conformal time and ϵ_{DDM}, and m_{DDM} are the energy, and mass of decaying dark matter. Following established procedure, we express the distribution function of species X as a zeroth-order distribution plus a perturbation,

$$f_{\rm X}(\vec{x},\vec{q},\tau) = f^0_{\rm X}(q,\tau)[1+\Psi_{\rm X}(\vec{x},\vec{q},\tau)] \tag{2.3}$$

The evolution of the mean energy density for DDM and its RD particles follow from the zeroth-order integrals of Eq. (2.1) and Eq. (2.2),

$$\dot{\rho}_{\rm DDM} + 3H\rho_{\rm DDM} = -a\Gamma\rho_{\rm DDM} \tag{2.4}$$

$$\dot{\rho}_{\rm RD} + 4H\rho_{\rm RD} = a\Gamma\rho_{\rm DDM} \tag{2.5}$$

Here and throughout, we designate $\dot{y}$ as the time derivative of y. In the limit of a massive DDM particle, evolution of the comoving density $\rho_{\rm DDM}a^3$ approaches $\exp(-\Gamma t)$.

We have modified the publicly-available `CMBFAST` code of Seljak and Zaldarriaga [68] to compute the potential or matter power spectra. As we noted in § 2.2, we quote the perturbation equations explicitly in synchronous gauge simply because `CMBFAST` is written in terms of the synchronous gauge perturbations. Gauge transformations can be made straightforwardly [67].

In the synchronous gauge, the Fourier transform of the Boltzmann equation can be written

$$\frac{\partial\Psi}{\partial\tau} + i\frac{q}{E}(\vec{k}\cdot\hat{n})\Psi + \frac{{\rm d}\ln f_0}{{\rm d}\ln q}\left[\dot{\eta} - \frac{\dot{h}+6\dot{\eta}}{2}(\hat{k}\cdot\hat{n})^2\right] = \frac{1}{f_0}\left(\frac{\partial f}{\partial\tau}\right)_C \tag{2.6}$$

The collision term, which is on the right hand side of Eq. (2.6) and describes the DDM decays, is proportional to $f^0_{\rm DDM}$, rendering the equations describing the evolution of DDM perturbations identical to those of standard, stable cold dark matter at the lowest order in perturbation theory. The perturbation equations describing the daughter particles are less trivial. Following [27] and [67], we expand the perturbation equations for RD particles in a series of Legendre polynomials $P_l(x)$, yielding

$$F_{\rm RD}(\vec{k},\hat{n},\tau) \;=\; \frac{\int dqq^3 f^0_{\rm RD}(q,\tau)\Psi_{\rm RD}}{\int dqq^3 f^0_{\rm RD}(q,\tau)} = \sum_{l=0}^{\infty}(-i)^l(2l+1)F_{{\rm RD},l}(\vec{k},\tau)P_l(\hat{k}\cdot\hat{n}), \tag{2.7}$$

where $F_{{\rm RD},l}(\vec{k},\tau)$ are the harmonic expansion coefficients. The orthonormality of Legendre polynomials allows the evolution equations to be written as

$$\dot{\delta}_{\rm RD} \;=\; -\frac{2}{3}(\dot{h}+2\theta_{\rm RD}) + a\Gamma\frac{\rho_{\rm DDM}}{\rho_{\rm RD}}(\delta_{\rm DDM}-\delta_{\rm RD}) \tag{2.8a}$$

$$\dot{\theta}_{\rm RD} \;=\; k^2\left(\frac{\delta_{\rm RD}}{4}-\sigma_{\rm RD}\right) - a\Gamma\frac{\rho_{\rm DDM}}{\rho_{\rm RD}}\theta_{\rm RD} \tag{2.8b}$$

$$\dot{\sigma}_{\rm RD} \;=\; \frac{2}{15}(2\theta_{\rm RD}+\dot{h}+6\dot{\eta}-\frac{9}{2}kF_{{\rm RD},3}) - a\Gamma\frac{\rho_{\rm DDM}}{\rho_{\rm RD}}\sigma_{\rm RD} \tag{2.8c}$$

$$\dot{F}_{\rm RD} = \frac{k}{2l+1}[lF_{{\rm RD},l-1} - (l+1)F_{{\rm RD},l+1}] - a\Gamma\frac{\rho_{\rm DDM}}{\rho_{\rm RD}}F_{{\rm RD},l},\ l \geq 3 \tag{2.8d}$$

at first order, where $\delta_{\rm RD} \equiv F_{\rm RD,1}$, $\theta_{\rm RD} \equiv 3/4kF_{\rm RD,1}$, $\sigma_{\rm RD} \equiv F_{\rm RD,2}$, and h is the scalar trace of the metric perturbation, all in well-established notation.

The growth of perturbation is affected by the change of energy density among the relativistic and non-relativistic components. From Eq. (2.4) and Eq. (2.5) we can see that in the decaying dark matter scenario the comoving dark matter density decreases exponentially, and all of this decrement is transferred into relativistic energy density. Consequently, perturbation growth exhibits a scale-dependent suppression relative to stable dark matter, where the relevant scale is the horizon size at the epoch of decay. This late-time suppression of structure growth in large part provides the necessary leverage for weak lensing constraints on unstable dark matter. For daughter particles, the additional ρ_{DDM}/ρ_{RD} terms have an impact on scales greater than the horizon at the time of decay [27].

As we will discuss below in § 2.2, some of the constraining power of weak gravitational lensing, which is the observable that we consider for this class of DDM, comes from observations made on scales where linear perturbation theory is no longer adequate (e.g., [69, 70, 71, 72, 73, 74]). The constraints we forecast in the following sections that are based on linear scales only are robust and interesting in and of themselves. However, the utility of weak lensing is greatly increased if scales modified by nonlinearity can also be exploited for cosmological constraints [74], so we explore multiple proposed nonlinear corrections to linear evolution in § 2.1.2.

We also consider a second class of model in which that dark matter decays into another species of stable dark matter with a small mass splitting, DDM $\rightarrow$ SDM + L, where L denotes a "massless" daughter particle, SDM is the stable dark matter with mass m, and DDM is the decaying dark matter with mass M. The mass loss fraction f of DDM is directly related to the kick velocity deposited to the SDM particle by $f \simeq V_k/c$ from energy-momentum conservation. The following relations are valid in the rest frame of DDM particles with the kick velocity of SDM being the velocity relative to the DDM rest frame.

Following the same approach as previous model, the rate of change in the DDM distribution function is

$$\dot{f}_{DDM}(q_{DDM}) = -\frac{a^2 M\Gamma}{E_{DDM}} f_{DDM}(q_{DDM}) \simeq -a\Gamma f_{DDM}(q_{DDM}), \tag{2.9}$$

where $\dot{f}$ denotes the partial derivative of the distribution function with respect to conformal time, $\mathrm{d}\tau = \mathrm{d}t/a$, Γ is the decay rate, a is the cosmological scale factor, q_{DDM} is the comoving momentum, and $E_{DDM} = \sqrt{q_{DDM}^2 + M^2 a^2}$. This is very similar to Eq. (2.1) in the previous model. Specializing to two-body decays, one can show that the corresponding change to the SDM distribution function will be [75, 19]

$$\dot{f}_{SDM}(p_{SDM}) = \frac{aM^2\Gamma}{2E_{SDM}\, p_{SDM}\, p_{CM}} \int_{E_i}^{E_f} dE\, f_{DDM}(p), \tag{2.10}$$

where

$$E_{f,i} = \frac{1}{2} E_{SDM} m_0^2 \pm p_{SDM} p_{CM} M/m_{SDM}^2,$$

the quantity p_{CM} is the center-of-mass momentum, and $m_0^2 \equiv M^2 + m^2$.

We again define the average distribution function, $f_i^0(q,\tau)$, and the perturbation to the distribution function, $\Psi_i(\vec{x},\vec{q},\tau)$, for each different species of particle according to Eq. (2.3) Since DDM particles are non-relativistic, their zero order phase-space distribution is the Maxwell-Boltzmann function. The zero order phase-space distribution function of SDM is [31, 19]

$$f_{0,SDM}(q,a) = \frac{\Gamma\Omega_M \rho_{crit}}{Mq^3 H(a')} \exp(-\Gamma t_q)\, \Theta(a p_{CM} - q) \tag{2.11}$$

where q is the comoving momentum of the SDM particle, $a' = q/p_{CM}$, and $t_q = t(a')$. This can be derived from the fact that the decay always generates SDM particles with the same physical momentum p_{CM}. In the SDM distribution function, the spectrum of different momenta arises from decays at different times, designated by the cosmic scale factor a' so that $q = p_{CM} a'$. The Heaviside step function $\Theta(a p_{CM} - q)$ (see Eq. 2.11) enforces a cut-off $q_{\max} = a p_{CM}$ at a given redshift a. This maximum momentum stems from the fact that the maximum momentum at a given redshift is from decay processes happening at that time,

while SDM with lower momenta are from the earlier decays. To be explicit, the average comoving number density of SDM particles is the integral of f_0 over momentum space,

$$n_{SDM} = \int q^2 \mathrm{d}q \, \mathrm{d}\Omega \, f_{0,SDM}(q) \tag{2.12}$$

$$\rightarrow \mathrm{d}n_{SDM}(q) = 4\pi q^2 \mathrm{d}q \, f_{0,SDM}(q) \tag{2.13}$$

Thus $f_{0,SDM}$ can be written as

$$f_{0,SDM}(q) = \frac{\mathrm{d}n_{SDM}(q)}{q^2 \mathrm{d}q} = \frac{\mathrm{d}n_{SDM}}{q^2 p_{CM} \mathrm{d}a'} = \frac{1}{H(a')q^3} \frac{\mathrm{d}n_{SDM}}{\mathrm{d}t'} \tag{2.14}$$

$$\rightarrow f_{0,SDM}(q) = \frac{1}{MH(a')q^3} \frac{\mathrm{d}(\rho_{DDM} a'^3)}{\mathrm{d}t'} \tag{2.15}$$

This then implies Eq. (2.11) after enforcing the maximum momentum at $q_{\max} = a p_{CM}$.

The evolution equations for the mean energy densities in the two dark matter components are given by the integrals of Eq. 2.9 and Eq. 2.10 using the unperturbed distribution function. They read

$$\dot{\rho}_{DDM} + 3\frac{\dot{a}}{a}\rho_{DDM} = -a\Gamma\rho_{DDM} \tag{2.16}$$

and

$$\dot{\rho}_{SDM} + 3\frac{\dot{a}}{a}(\rho_{SDM} + P_{SDM}) = \Gamma\frac{a m_0^2}{2M^2}\rho_{DDM} \tag{2.17}$$

respectively. Given the DDM energy density, the decay product energy density $\rho_d = \rho_{SDM} + \rho_L$ can be obtained using the first law of thermodynamics [76, 77] from

$$\frac{\mathrm{d}a^3\rho_d}{\mathrm{d}\tau} = -P_d\frac{\mathrm{d}a^3}{\mathrm{d}\tau} - \frac{\mathrm{d}(a^3\rho_{DDM})}{\mathrm{d}\tau}. \tag{2.18}$$

This implies that the energy density evolution of the massless daughter particle L is

$$\dot{\rho}_L + 3\frac{\dot{a}}{a}(\rho_L + P_L) = \dot{\rho}_L + 4\frac{\dot{a}}{a}\rho_L = \Gamma\frac{a(M^2 - m^2)}{2M^2}\rho_{DDM} \tag{2.19}$$

To compute the matter power spectra, it is necessary to compute the perturbations to the dark matter distributions and the metric. Our treatment of perturbations again follows the conventions established in Ma and Bertschinger [78]. We will present our results in the synchronous gauge, because this choice lends itself to numerical evaluation using publicly-available `CMBFAST` code [68] or `CAMB` [79]. The same as the previous model, the

DDM perturbation equations are the same as the well-known equations describing CDM. For the decay products, the collision terms are

$$\left(\frac{\partial f_{SDM}}{\partial \tau}\right)_C = \frac{a m_0^2 \Gamma}{2ME} f_{0,DDM}(1+\Psi_{DDM}) \tag{2.20}$$

and

$$\left(\frac{\partial f_L}{\partial \tau}\right)_C = \frac{a(M^2-m^2)\Gamma}{2ME} f_{0,DDM}(1+\Psi_{DDM}). \tag{2.21}$$

The factors $m_0^2/(2M^2)$ and $(M^2-m^2)/(2M^2)$ that appear in the SDM and L collision terms can be easily understood. Consider a two-body decay in the rest frame of the DDM particle, $A \to B + C$, with corresponding masses m_A, m_B, and m_C. The energies of B and C in the rest frame of A are $E_B = (m_A^2 + m_B^2 - m_C^2)/(2m_A)$ and $E_C = (m_A^2 + m_C^2 - m_B^2)/(2m_A)$. So these factors represent the ratios of energy that have been deposited into different daughter particle species.

The perturbations for the massless relativistic daughter particles may be treated in a manner analogous to that of massless neutrinos, save for the peculiar distribution function of the L. Following the treatment of relativistic daughter (RD) particles in previous mode and evaluating the Boltzmann equation for our Legendre polynomial expansion as in Eq. (2.7) yields the evolution of the multipole coefficients in the conventional notation,

$$\dot{\delta}_{\rm L} = -\frac{2}{3}(\dot{h}+2\theta_{\rm L}) + a\Gamma\frac{E_2}{M}\frac{\rho_{\rm DDM}}{\rho_{\rm L}}(\delta_{\rm DDM}-\delta_{\rm L}), \tag{2.22}$$

$$\dot{\theta}_{\rm L} = k^2(\frac{\delta_{\rm L}}{4}-\sigma_{\rm L}) - a\Gamma\frac{E_2}{M}\frac{\rho_{\rm DDM}}{\rho_{\rm L}}\theta_{\rm L}, \tag{2.23}$$

$$\dot{\sigma}_{\rm L} = \frac{2}{15}(2\theta_{\rm L}+\dot{h}+6\dot{\eta}-\frac{9}{4}kF_{\rm L,3}) - a\Gamma\frac{E_2}{M}\frac{\rho_{\rm DDM}}{\rho_{\rm L}}\sigma_{\rm L}, \tag{2.24}$$

and

$$\dot{F}_{\rm L,l} = \frac{k}{2l+1}[lF_{{\rm L},l-1} - (l+1)F_{{\rm L},l+1}] - a\Gamma\frac{E_2}{M}\frac{\rho_{\rm DDM}}{\rho_{\rm L}}F_{{\rm L},l},\ l \geq 3, \tag{2.25}$$

Here we have defined $E_1 = (M^2+m^2)/(2M) = m_0^2/(2M)$ and $E_2 = (M^2-m^2)/(2M)$.

The SDM must be treated differently to account for their finite mass and non-trivial velocity kicks. We expand the perturbation to the distribution function, Ψ, in a Legendre series

$$\Psi(\vec{k},\hat{n},q,\tau)=\sum_{l=0}^{\infty}(-\imath)^l(2l+1)\Psi_l(\vec{k},q,\tau)P_l(\hat{k}\cdot\hat{n}). \tag{2.26}$$

We have dropped the "SDM" subscript on Ψ for brevity as there should be no cause for confusion in this context. Evaluating the Boltzmann evolution equation on this expansion, we obtain for the different multipoles

$$\frac{\partial\Psi_0}{\partial\tau}=-\frac{qk}{E}\Psi_1+\frac{1}{6}\dot{h}\frac{d\ln f_{SDM,0}}{d\ln q}+a\Gamma\frac{E_1}{E}\frac{f_{DDM,0}}{f_{SDM,0}}\Psi_{DDM,0}-a\Gamma\frac{E_1}{E}\frac{f_{DDM,0}}{f_{SDM,0}}\Psi_0, \tag{2.27}$$

$$\frac{\partial\Psi_1}{\partial\tau}=\frac{qk}{3E}(\Psi_0-2\Psi_2)-a\Gamma\frac{E_1}{M}\frac{f_{DDM,0}}{f_{SDM,0}}\Psi_1, \tag{2.28}$$

$$\frac{\partial\Psi_2}{\partial\tau}=\frac{qk}{5E}(2\Psi_1-3\Psi_3)-(\frac{1}{15}\dot{h}+\frac{2}{5}\dot{\eta})\frac{df_{SDM,0}}{dlnq}-a\Gamma\frac{E_1}{E}\frac{f_{DDM,0}}{f_{SDM,0}}\Psi_2, \tag{2.29}$$

and

$$\frac{\partial\Psi_l}{\partial\tau}=\frac{qk}{(2l+1)E}(l\Psi_{l-1}-(l+1)\Psi_{(l+1)})-a\Gamma\frac{E_1}{M}\frac{f_{DDM,0}}{f_{SDM,0}}\Psi_l. \tag{2.30}$$

for $l\geq 3$.

If we restrict attention only to cases in which the mass difference between the DDM and SDM particles is small, $f=1-m/M\ll 1$, the SDM particle will receive an extremely non-relativistic kick velocity $V_k\sim fc$. As we should expect, SDM behaves similarly to CDM, aside from the fact that it is endowed with a non-negligible distribution of momentum due to the DDM decays. In this limit, the SDM perturbations evolve as for a standard non-relativistic dark matter species,

$$\dot{\delta}_{SDM}=-\theta_{SDM}-\frac{1}{2}\dot{h}+a\Gamma\frac{E_1}{M}\frac{\rho_{DDM}}{\rho_{SDM}}(\delta_{DDM}-\delta_{SDM}) \tag{2.31}$$

and

$$\dot{\theta}_{SDM}=-\frac{\dot{a}}{a}\theta_{SDM}+\frac{\delta P_{SDM}}{\delta\rho_{SDM}}k^2\delta_{SDM}-a\Gamma\frac{E_1}{M}\frac{\rho_{DDM}}{\rho_{SDM}}\theta_{SDM}, \tag{2.32}$$

where

$$c_s^2=\frac{\delta P_{SDM}}{\delta\rho_{SDM}}=\frac{\frac{4\pi}{3}a^{-4}\int q^2dq\frac{q^2}{E}f_0(q)\Psi_0}{4\pi a^{-4}\int q^2dqEf_0(q)\Psi_0} \tag{2.33}$$

The higher multipole terms become negligible in the non-relativistic as they are proportional to powers of the ratio of the kinetic energy to the total energy, q/ϵ.

Though we solve the complete equations for the evolution of the SDM perturbations, the non-relativistic kick velocity approximation is valid in most of our calculations. The most interesting constraints from future surveys are relevant for models with $V_k \leq 10^{-3}c$ and relativistic kicks have already been ruled out for a wide range of lifetimes [80, 30].

Perturbation growth is suppressed on scales smaller than the *free-streaming* scale. The free-streaming scale is, in turn, determined by an integral of the sound speed c_s. We defer a detailed discussion of the free-streaming scale in our decaying dark matter models and its imprint on the matter, weak lensing, and Lyman-α forest power spectra to § 3.

2.1.2 Non-linear correction for decaying dark matter models

Our most robust constraints stem from perturbations on linear scales. However, it is interesting to estimate the level of constraints that may be achieved by exploiting mildly non-linear scales as is common practice in the established framework for exploring dark energy with lensing and galaxy clustering statistics [81]. Including mildly nonlinear scales improves constraints because it increases the signal-to-noise of lensing measurements and because it includes information regarding the effects of DDM on the abundance and internal structures of cluster-sized dark matter halos. We explore constraints including mildly nonlinear scales as a means of estimating the level of constraints that may be achievable after an exhaustive numerical simulation program, similar to what is being performed for dark energy [82].

We implement the nonlinear corrections to the matter and lensing power spectra using the halo model [83]. The halo model is known to exhibit mild systematic offsets compared to numerical simulations and the nonlinear correction of [84]. However, we use the halo model because it provides a convenient framework for estimating the alterations to nonlinear structure induced by DDM before performing an exhaustive numerical investigation. We combine the standard aspects of the halo model with an analytical model proposed by Peter [80] for the first DDM model and Sánchez-Salcedo [18] for the second one for the alterations to dark matter halo structure due to the decay process.

The halo model (see [83] for a review) is based on the assumption that all matter resides within dark matter halos. The matter power spectrum is given by the sum of two terms,

$$P(k) = P_{1H}(k) + P_{2H}(k), \tag{2.34}$$

where

$$P_{1H}(k) = \frac{1}{\rho_M^2} \int dm\, m^2 \frac{dn}{dm} \lambda^2(k|m), \tag{2.35}$$

and

$$P_{2H}(k) = \frac{1}{\rho_M^2} P^{\rm lin}(k) \left[\int dm\, m \frac{dn}{dm}\, \lambda(k|m)\, b_h(m) \right]^2. \tag{2.36}$$

In the foregoing equations, ρ_m is the mean matter density of the universe, m is halo mass, $\lambda(k|m)$ is the Fourier transform of the NFW density profile for a halo mass m, $P^{\rm lin}(k)$ is the linear matter power spectrum, and $b_h(m)$ is the halo bias function. The one-halo term $P_{1H}(k)$, describes correlations among mass elements within a common halo while the two-halo term $P_{2H}(k)$, is due to correlations among mass elements in distinct halos.

For the first class of model, to estimate the impact of decaying dark matter on matter clustering we follow the approach denoted as *Case 1* by [80] to describe modifications to the halo mass function, halo bias, and internal halo structure. We then incorporate these modifications into the halo model formulae of Eq. (2.35) and Eq. (2.36) to compute lensing power spectra. This model is based upon the assumption that halos at early times are very much like their counterparts in models of stable, cold dark matter (because little decay will occur in any viable model) and that modifications to halo structure can be described by the conservation of adiabatic invariants describing dark matter particle orbits.

Consider a population of dark matter halos that formed prior to any significant dark matter decays such that halos at any time $t \ll H_0^{-1}$ can be modeled as standard, CDM halos. These halos then lose mass as their constituent dark matter particles decay. If the decay lifetime is much larger than the halo dynamical timescale (as it will always be in cases of interest because dynamical times are $\tau_{\rm dyn} \leq 0.1 H_0^{-1}$ and viable regions of parameter space are $\Gamma^{-1} \gg H_0^{-1}$), then the halo gravitational potential changes adiabatically. Exploiting the adiabatic invariance of angular momentum for particles on nearly circular orbits, establishes

a prediction for the relationship between the initial and final matter distribution within a dark matter halo,

$$M_i(r_i)r_i = M_f(r_f)r_f, \tag{2.37}$$

where $M_i(r)$ is the mass enclosed within radius r in the initial, early-time halo, $M_f(r)$ is the corresponding quantity describing the contemporary, late-time halo, and r_i and r_f are the initial and final radii of a particle shell, assuming that mass shells never cross and particles move in circular orbits. Eq. (2.37) is the basic relation of the standard, adiabatic contraction model for predicting modifications of halo structure due to collisional processes [85, 46, 47].

For unstable dark matter, with a lifetime τ_{ddm}, a fraction $f(\tau_{ddm}, z)$ of unstable dark matter particles will have decayed by redshift z. According to the adiabatic contraction model, the mass enclosed in r_f will be

$$M_f(r_f) = (1 - f(\tau_{ddm}, z))M_i(r_i) \tag{2.38}$$

Inserting Eq. (2.38) into Eq. (2.37), the relationship between the initial and final radii is

$$r_f = r_i/(1 - f(\tau_{ddm}, z)). \tag{2.39}$$

If we assume that the initial dark matter halos can be well described by NFW profiles, the final mass distribution will be

$$\rho_f(r_f) = \frac{1}{4\pi r_f^2}\frac{dM_f}{dr_f} \tag{2.40}$$

$$= \frac{(1-f)^2}{4\pi r_f^2}\frac{dM_i}{dr_i} \tag{2.41}$$

$$= \frac{(1-f)^4\rho_s}{\left(\frac{(1-f)r_f}{r_s}\right)\left[1+\frac{(1-f)r_f}{r_s}\right]^2}. \tag{2.42}$$

We model the initial mass function dn_i/dm and halo bias $b_h(m)$ using the relations of [86]. This choice is made for convenience because in models with stable dark matter, it satisfies the necessary conditions that the halo model integrals contain all mass and that the clustering of dark matter is unbiased with respect to itself. Some definitions of halo virial radii will be altered by decays. In order to ensure that all mass remains accounted for, we define halos as the mass within virial radii fixed to a definition of 200 times the average

density of the Universe in the absence of decays. Thus, virial radii are fixed to be the same as they would be in standard CDM, but halo masses are smaller by a factor of $1 - f(\Gamma^{-1}, z)$. This definition preserves the convenient properties of the bias and mass relations in [86] and is identical to their halo definition in the absence of dark matter decays.

The new halo mass function at mass M_f is

$$\frac{dn_f(M_f, z)}{dm} = \frac{dn_i(M_i, z)}{dm} \tag{2.43}$$

and

$$b_h(M_f) = b_h(M_i), \tag{2.44}$$

where the initial and final masses are related via Eq. (2.38). In other words, we assume the abundance and clustering to follow the abundance and clustering laws for halos of stable dark matter of the corresponding masses. Notice that the abundance of halos of a given contemporary mass M_f is reduced compared to that in a stable dark matter model because the final mass reflects the mass loss due to decays and more massive halos are intrinsically rare. Likewise, halos of final mass M_f are more strongly clustered than their counterparts in stable dark matter scenarios because halo bias is an increasing function of mass (see [87] for the basic theory of the mass function and bias). The halo density profiles also become shallower as r_s increases and ρ_s decreases when the decay-induced modifications to halo profiles are accounted for. The reduction in the number of halos and the shallowing of halo profiles reduces lensing power compared to a halo model with no accounting for mass loss. As we show in § 3, this additional reduction in power is a distinctive feature that leads to slightly more restrictive bounds on DDM lifetimes.

In the second class of DDM model, dark matter halos also begin with the same density profiles as in the standard CDM model for relevant lifetimes ($\Gamma^{-1} \gg H_0^{-1}$). Their density distributions can be well described by Navarro et al. [88] (NFW) profiles. As the DDM decays, the kinetic energy of dark matter particles will change because SDM particles receive a small kick velocity from their parent particles. Assuming that we only consider decay processes with $f \ll 1$, the mass of the parent and daughter particles will be nearly identical. As discussed in Sánchez-Salcedo [18], *on average* the net effect of decays is to impart an amount of energy $\Delta E \approx m v_k^2/2$ on the dark matter, independent of the initial velocity.

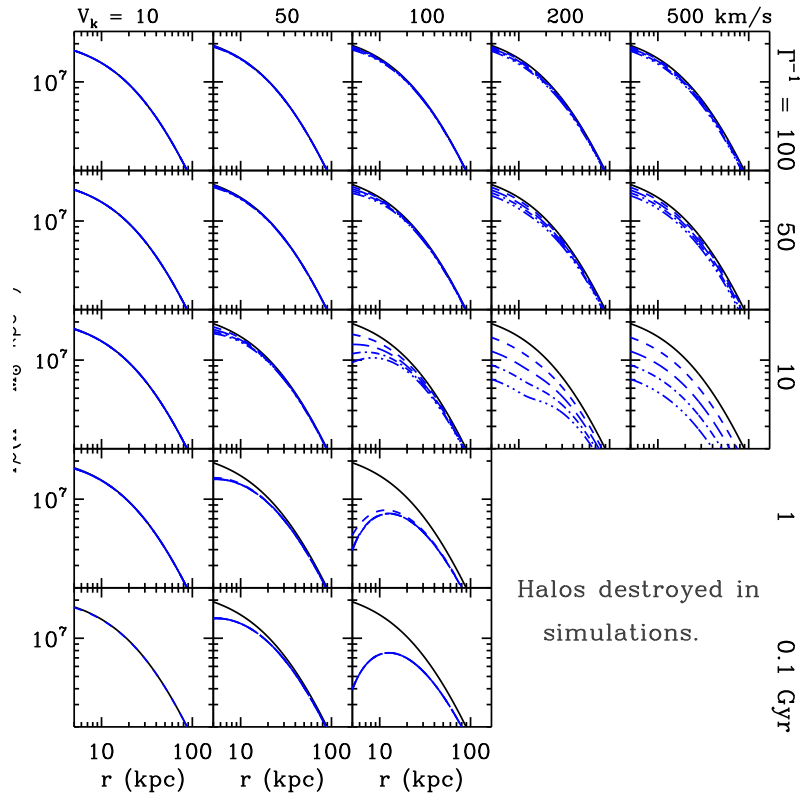

Figure 2.1: Dark matter density profiles times radius, $r\,\rho(r)$, as a function of radius and time. The dark matter halo mass is $M_{\rm h} = 10^{12}\,{\rm M}_\odot$. In the absence of dark matter decays, the halo concentration is $c = 5$. The halo has a virial speed $v_{vir} \equiv \sqrt{GM_{\rm h}/R_{vir}} \approx 130$ km/s. Different panels are for different choices of kick velocity and lifetime as labeled along the top and right axes respectively. In each panel the solid lines show the initial NFW profile. The short-dashed line, long-dashed line, dash-dotted line, and dash-double-doted line represent density profiles after 2.5, 5, 7.5, and 10 Gyr. This figure is designed to be directly comparable to the simulation results displayed in Fig. 1 of [29].

The changes in average kinetic energy will result in changes in particle orbits, causing an expansion of dark matter halos and a shallowing of dark matter profiles.

To demonstrate the effect of density profile modification, we adopt a two-step calculation.

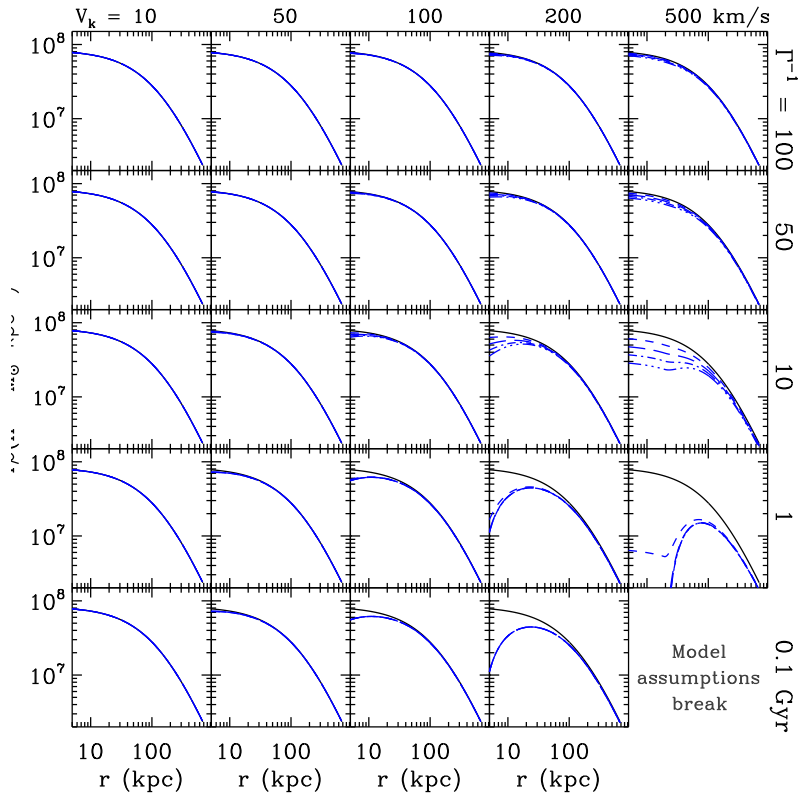

Figure 2.2: Similar to Figure 2.1 but for halos with $M_{\rm h} = 5 \times 10^{13}\,{\rm M}_{\odot}$ and NFW concentration c=5. The halo virial speed is $v_{vir} \approx 477$ km/s.

Assume that DDM particles in halos follow circular orbits prior to any significant DDM decays. The particles orbit in the gravitational potential of the NFW halo, which can be approximately described by a power law $v_c(r) = v_0(r/r_0)^{1/2\beta}$ over any sufficiently small range of r. In a given time interval, a small fraction of DDM particles decay and their daughter SDM particles gain a small amount of energy $\Delta E \approx mv_k^2/2$. In general, the daughter particles will move from circular orbits to elongated orbits, characterized by the new energy relative to the halo potential and an apocentric radius r. Orbits in the NFW potential are not closed, rendering it a numerical problem to compute the time-averaged value of the radial coordinate of the daughter particle. To obtain a simplistic estimate of the new radii

the particles move to, we assume that the new average position of the daughter is similar to the radius of a circular orbit at the new value of the orbital energy. This is *conservative* in the present context, because circular orbits in equilibrium are *least* susceptible to such expansion [18]. In this assumption, the radial position of the daughter particles, r', will be

$$r' = \left(r^{1/\beta} + \frac{1}{2\beta + 1} \left(\frac{v_k(R)}{v_0} \right)^2 r_0^{1/\beta} \right)^{\beta} . \tag{2.45}$$

The model we have described is not self-consistent, so it is important to validate the basic predictions of the model against more complete calculations. To check the validity of this model, we compare our analytical calculation results with the N-body simulation results from [29]. In Figure 2.1, we plot density profiles for a dark matter halo with mass $M_{\rm h} = 10^{12}\,{\rm M}_\odot$ and an initial NFW concentration parameter $c = 5$ for several different lifetimes and kick velocities. Peter et al. [29] computed the profiles of dark matter halos in the same model using N-body simulations that accounted for the dark matter decays. Fig. 2.1 is the same as Figure 1 in Peter et al. [29] save for the fact that we have computed modified halo profiles according to the analytic model described in this section. A comparison of the two figures reveals that the analytic model and the numerical simulations are in remarkable agreement for all models with $V_k \lesssim$ 200km/s and $\Gamma^{-1} \gtrsim$ 10 Gyr. There are several possible explanations for the inconsistencies that arise when $V_k \gtrsim$ 200 km/s and $\Gamma^{-1} \lesssim$ 10 Gyr. One is that when changes to the gravitational potential are not small, the final gravitational potential is sufficiently different from the initial gravitational potential that the initial potential cannot be used to approximate the new positions of the SDM particles. Another possibility is that typical circular orbits no longer provide useful approximations for the degree of halo expansion. As discussed in [29], where they look at velocity anisotropy of their simulated halos, they found that the orbits become radially biased at the halo outskirts. Moreover, $V_k = 200$ km/s is considerable compared to the virial velocity of a $M_{\rm h} = 10^{12}\,{\rm M}_\odot$ halo, so it is not surprising that those halos are not in dynamical equilibrium for large V_k and small lifetime. These simulation results show that the assumptions of our simple model are violated in the regime of high kick velocity and low lifetime. As we show in § 3, our primary results in which the nonlinear model is used correspond to $V_k \lesssim$ 200km/s and lifetimes $\Gamma^{-1} \gtrsim$ 100Gyr, so our use of this model for a first foray into this regime is justified.

Unlike Peter et al. [29], we are interested in cosmological weak lensing as our observable. The halo mass most relevant to weak lensing lie in the range $M_{\rm h} \approx 10^{13} - 10^{14} M_{\odot}$ [74]. Such halos have significantly larger virial velocities than the $10^{12}\,{\rm M}_{\odot}$ halos considered above. Typical virial velocities of these larger halos lie in the range $v_{vir} \approx 280 - 600$ km/s. This suggests that our model can be used at larger V_k than the value $V_k \approx 200$ km/s that we arrived at by comparing to simulations of a $10^{12}\,{\rm M}_{\odot}$ halo above, because these kicks represent a smaller fraction of the potential well depth. For instance, Peter et al. [29] pointed out that the cluster mass function is insensitive to $V_k \lesssim 500$ km/s, because the typical virial speeds clusters are $V_k \gtrsim 600$ km/s. For completeness, we show the corresponding density profile modifications for these group- and cluster-sized halos in Figure 2.2. We will show in § 3 that our calculations are only sensitive to DDM parameters that result in density profiles with mild changes.

We include this effect in our nonlinear halo model calculation by giving all recomputing halo profiles or halo mass function as described above. We modified halo profiles by assuming initial halos with the same profiles, including concentrations, as their concordance ΛCDM counterparts and implementing the above model on these halos. Ideally, one would treat nonlinear corrections to structure growth using program of cosmological numerical simulations. However, we place such a study outside the scope of the present work as our initial aim is to estimate the constraining power of forthcoming surveys. In this manner, we estimate the fruit that a computationally-intensive numerical simulation program may bear on the problem of unstable dark matter.

2.2 WEAK LENSING

Weak lensing as a cosmological probe has been discussed at length in numerous papers (a recent review is [89]). We give a brief description of our methods below, which are mostly based on the conventions and notation in [74]. In the first class of DDM model where the decay process may generate certain amount of relativistic energy at late time, we consider the linear evolution of full metric potential in the lensing power spectrum instead of using

matter-domenated assumption as in [74]. In this manner, our work is very similar in spirit to that of Schmidt [73]. The most robust forecasts derive from considerations of possible weak lensing measurements restricted to scales where linear perturbative evolution of the metric potentials remains useful. However, we attempt to estimate possible improvements to the constraining power of weak lensing observables, provided that mildly nonlinear evolution can be modeled robustly.

First I will explain the weak lensing model using the convention of [74], and then I will demonstrate how to convert into the full potential form, which is actually more integrated and will converge back to the notation in [74] in the matter-dominated universe. We consider the set of observables that may be available from large-scale galaxy imaging surveys to be the auto- and cross-spectra of lensing convergence from sets of galaxies in $N_{\rm TOM}$ redshift bins. The $N_{\rm TOM}(N_{\rm TOM}+1)/2$ distinct convergence spectra are

$$P_\kappa^{\rm ij}(\ell) = \int {\rm d}z \frac{W_{\rm i}(z) W_{\rm j}(z)}{H(z) D_A^2(z)} P_m(k=\ell/D_{\rm A}, z), \tag{2.46}$$

where i and j label the redshift bins of the source galaxies. We take $N_{\rm TOM}=5$ and evenly space bins in redshift from a minimum redshift of $z=0$ to a maximum redshift of $z=3$. Increasing the number of bins beyond $N_{\rm TOM}=5$ adds only negligibly to the constraining power of lensing data, in accord with an analogous statement for dark energy constraints [90].In Eq. (2.46), $H(z)$ is the Hubble expansion rate, $D_A(z)$ is the comoving angular diameter distance, and $P_m(k,z)$ is the matter power spectrum at wavenumber k and redshift z.

The W_i are the lensing weight functions for source galaxies in redshift bin i. In practice, the galaxies will be binned by photometric redshift, so that the bins will have non-trivial overlap in true redshift (see [90, 91] for detailed discussions). Defining the true redshift distribution of source galaxies in the ith photometric redshift bin as dn_i/dz, the weights are

$$W_i(z) = \frac{3}{2}\Omega_M H_0^2 (1+z) D_A(z) \int dz' \frac{D_A(z,z')}{D_A(z')} \frac{dn_i}{dz'} \tag{2.47}$$

where $D_A(z,z')$ is the angular diameter distance between redshift z and z' and H_0 is the present Hubble rate.

If we consider the full potential metric, convergence spectra will take the following form

$$P_{\kappa,pot}ij(\ell) = \ell^4 \int \mathrm{d}z \frac{W_\mathrm{i}(z)W_\mathrm{j}(z)}{H(z)D_A^6(z)} P_{\Psi-\Phi}(k = \ell/D_\mathrm{A}, z), \tag{2.48}$$

where $P_{\Psi-\Phi}(k, z)$ is the power spectrum of Newtonian gauge scalar potentials $\Psi - \Phi$ at wavenumber k and redshift z. The difference in Eq. (2.46) and Eq. (2.48) is in the way we describe the potential field where the presence of matter potential bend the light from background galaxies. They can be converted back and forth using Poisson's equation. In this notation the window functions are

$$W_{i,pot}(z) = D_A \int dz' \frac{D_A(z, z')}{D_A(z')} \frac{dn_i}{dz'} \tag{2.49}$$

We model the uncertainty induced by utilizing photometric galaxy redshifts with the probability function of assigning an individual source galaxy photometric redshift z_p given a true redshift z, $P(z_p|z)$. The true redshift distribution of sources in the ith photometric redshift bin is

$$\frac{dn_i(z)}{dz} = \int_{z_{p,i}^{(low)}}^{z_{p,i}^{(high)}} dz_p \; \frac{dn(z)}{dz} \; P(z_p|z) \tag{2.50}$$

Here we take the true redshift distribution to be

$$\frac{dn(z)}{dz} = \bar{n} \frac{4z^2}{\sqrt{2\pi z_0^3}} \exp[-(z/z_0)^2] \tag{2.51}$$

with $z_0 \simeq 0.92$, so that the median survey redshift to $z_{med} = 1$, and $\bar{n}$ as the total density of source galaxies per unit solid angle [92, 93, 94]. We assume that uncertain photometric redshifts can be approximated by taking

$$P(z_p|z) = \frac{1}{\sqrt{2\pi\sigma_z}} \exp\left[-\frac{(z_p - z)^2}{2\sigma_z^2}\right] \tag{2.52}$$

where $\sigma_z(z) = 0.05(1 + z)$ [90]. Complexity in photometric redshift distributions is an issue that must be overcome to bring weak lensing constraints on cosmology to fruition (e.g., [95, 91]).

Observed convergence power spectra $\bar{P}_\kappa^{ij}(\ell)$, contain both signal and shot noise,

$$\bar{P}_\kappa^{ij}(\ell) = P_\kappa^{ij} + n_i \delta_{ij} \langle \gamma^2 \rangle \tag{2.53}$$

where $\langle\gamma^2\rangle$ is the noise from intrinsic ellipticities of source galaxies, and n_i is the surface density of galaxies in the ith tomographic bin. We follow recent convention and set $\sqrt{\langle\gamma^2\rangle} = 0.2$, subsuming additional errors on galaxy shape measurements into an effective mean number density of galaxies, $\bar{n}$. Assessments of intrinsic shape noise per galaxy may be found in, for example [96, 97, 98]. Assuming Gaussianity of the lensing field, the covariance between observables $\bar{P}_\kappa^{ij}$ and $\bar{P}_\kappa^{kl}$ is

$$C_{AB} = \bar{P}_\kappa^{ik}\bar{P}_\kappa^{jl} + \bar{P}_\kappa^{il}\bar{P}_\kappa^{jk} \tag{2.54}$$

where the i and j map to the observable index A, and k and l map to B such that C_{AB} is a square covariance matrix with $N_{\rm TOM}(N_{\rm TOM}+1)/2$ rows and columns. We assume Gaussianity throughout this work and even in our most aggressive forecasts we consider only multipoles $\ell < 3000$, at which point the Gaussian assumption and several weak lensing approximations break down [69, 99, 100, 101, 102].

2.2.1 Forecasting methods

The Fisher Information Matrix provides a simple estimate of the parameter covariance given data of specified quality. The Fisher matrix has been utilized in numerous, similar contexts in the cosmology literature [103, 104, 105, 106, 107, 72, 74, 108, 109, 95, 21, 22], so we give only a brief review of important results and the caveats in our particular application. We have confirmed the validity of the Fisher matrix approximation in models of unstable dark matter using Monte Carlo methods as described in [21].

The Fisher matrix of observables in Eq. (2.46), subject to covariance as in Eq. (2.54), can be written as

$$F_{ij} = \sum_{\ell=\ell_{min}}^{\ell_{max}} (2\ell+1) f_{sky} \sum_{A,B} \frac{\partial P_{\kappa,A}}{\partial p_i} [C^{-1}]_{AB} \frac{\partial P_{\kappa,B}}{\partial p_j} + F_{ij}^P \tag{2.55}$$

where the indices A and B run over all $N_{\rm TOM}(N_{\rm TOM}+1)/2$ spectra and cross spectra, the p_i are the parameters of the model, f_{sky} is the fraction of the sky imaged by the experiment, and $\ell_{min} = 2f_{sky}^{-1/2}$ is the smallest multipole constrained by the experiment. F_{ij}^P is a prior Fisher matrix incorporating previous knowledge of viable regions of parameter space. We set $\ell_{max} = 300$ for linear forecasts and $\ell_{max} = 3000$ in our most ambitious nonlinear forecasts.

On smaller scales (higher ℓ), various assumptions, such as the Gaussianity of the lensing field, break down [69, 99, 100, 101, 102, 74, 49]. To be conservative, we explore modest priors on each parameter independently, so that $F_{ij}^P = \delta_{ij}/(\sigma_i^P)^2$, where σ_i^P is the 1σ prior on parameter p_i. The forecast, 1σ, marginalized constraint on parameter p_i is $\sigma(p_i) = \sqrt{[F^{-1}]_{ii}}$.

Our DDM models have one or two independent parameters, namely decay rate Γ (or lifetime, Γ^{-1}) for both model and mass loss fraction f (which is related to V_k via $V_k = fc$) for the second model. For the second class of DDM model, either one of these parameters can independently be tuned to render the effects of DDM negligible. So it is not useful to marginalize over one parameter to derive constraints on the other. In what follows, we choose to illustrate the effectiveness of lensing to constrain DDM by fixing lifetime and quoting possible constraints on f. Other than the decay model parameters, we also consider six cosmological parameters that we expect to modify weak lensing power spectra at significant levels and to exhibit partial degeneracy with our model parameters. We construct our forecasts for DDM parameter bounds after marginalizing over the remaining parameters. Our six additional parameters and their fiducial values (in parentheses) are the dark energy density Ω_Λ (0.74), the present-day dark matter density, $\omega_{\rm DM} = \Omega_{\rm DM}h^2$ (0.11), the baryon density $\omega_b = \Omega_b h^2$ (0.023), tilt parameter n_s(0.963), the natural logarithm of the primordial curvature perturbation normalization $\ln(\Delta_R^2)$ (-19.94), and the sum of the neutrino masses $\sum_i m_{\nu_i}$ (0.05 eV). This choice of fiducial model implies a small-scale, low-redshift power spectrum normalization of $\sigma_8 \simeq 0.82$. The optical depth to reionization has a negligible effect on the lensing spectra on scales of interest, so we do not vary it in our analysis.

We take priors on our cosmological parameters of $\sigma(\omega_m) = 0.007$, $\sigma(\omega_b) = 1.2 \times 10^{-3}$, $\sigma(\ln \Delta_R^2) = 0.1$, $\sigma(n_s) = 0.015$, and $\sigma(\Omega_\Lambda) = 0.03$. We assume no priors on DDM model parameters or neutrino mass. Our fiducial model is motivated by the WMAP seven-year result and our priors represent marginalized uncertainties on these parameters based on the WMAP seven-year data [4]. These priors are very *conservative* and allow for weaker constraints on DDM than would be expected from future data, where stronger priors may be available. To estimate the potential power of lensing constraints on DDM when stronger cosmological constraints are available, we also explore prior constraints on these parameters

at the level expected from the Planck mission[1] using the entire Planck prior Fisher matrix of [110]. Of course, using published priors from other analyses is not self-consistent because these priors were derived in analyses that assume stable dark matter, but for relevant lifetimes the dark matter decays should cause only subtle alterations to the cosmic microwave background anisotropy spectrum so this analysis should approximate a self-consistent simultaneous analysis of all data.

In some cases, we will estimate *nonlinear* power spectra in models with significant neutrino masses. In such cases, we follow the empirical prescription established in previous studies (e.g., [111, 108, 112]) and take

$$P_m(k) = \left[f_\nu \sqrt{P_\nu^{\rm lin}(k)} + f_{b+DM} \sqrt{P_{b+DM}^{NL}(k)} \right]^2 \tag{2.56}$$

where

$$f_\nu = \frac{\Omega_\nu}{\Omega_m}, \tag{2.57a}$$

$$f_{\rm b+DM} = \frac{\Omega_{\rm DM} + \Omega_b}{\Omega_m}, \tag{2.57b}$$

$P_\nu^{\rm lin}(k)$ is the linear power spectrum of neutrinos, and $P_{\rm b+DM}^{\rm NL}(k)$ is the nonlinear power spectrum evaluated for baryons and dark matter only. However, we note that recent work has questioned the robustness of this treatment of neutrino mass using direct numerical simulations [113] and perturbation theory [114], so it may become necessary to revisit this aspect of the modeling of power spectra prior to the availability of observational data.

We explore possible constraints from a variety of forthcoming data sets. We consider the Dark Energy Survey (DES) as a near-term imaging survey that could provide requisite data for this test. We model DES by taking a fractional sky coverage of $f_{sky} = 0.12$ and with $\bar{n} = 15/\text{arcmin}^2$. Second, we consider a class of future "Wide" surveys as may be carried out by the Large Synoptic Survey Telescope (LSST)[98] or Euclid [115]. We model these Wide surveys with $f_{sky} = 0.5$ and $\bar{n} = 50/\text{arcmin}^2$. Lastly, we consider a comparably narrow, deep imaging survey. We refer to such a survey as a "Deep" survey and model it with $f_{sky} = 0.05$ and $\bar{n} = 100/\text{arcmin}^2$. Such a survey may be more typical of a space-based mission similar

[1] `http://www.esa.int/planck`

to the proposed Wide-Field InfraRed Survey Telescope (WFIRST). In all cases, we take $\sqrt{\langle\gamma^2\rangle} = 0.2$ and assume particular shape measurement errors from each experiment are encapsulated in their effective number densities, in accord with recent conventional practice in this regard. Our results are relatively insensitive to number density because shot noise does not dominate cosmic variance on the scales we consider, and our linear constraints are completely insensitive to the choice of galaxy number density over a wide range.

2.3 LYMAN-α FOREST METHODS

The Lyman-α forest is a dense set of absorption features presented in quasi-stellar object (QSO) spectra. These features are caused by photoionized intergalactic medium (IGM) which are neutral hydrogen clouds around redshift z $\sim$ 2-4. Because these gaseous structures responsible for typical Lyman-α forest lines are large ($\gtrsim$ 100 kpc), low density ($\delta\rho/\rho \lesssim$ 10), and fairly cool (T $\sim 10^4$ K), pressure forces are sub-dominant, and the gas density closely traces the total matter density on large scales. The Fourier-transfered Lyman-α flux power spectrum $P_F(k, z)$ thus provides a way to estimate the matter fluctuation of scale up to around k$\sim$ a few hMpc^{-1} at high redshift.

In order to predict $P_F(k, z)$ for a given cosmological model, it is usually done by performing hydrodynamic simulations. In our case we used pure Smoothed-particle hydrodynamics (SPH) dark matter simulations, assuming gas and dark matter have the same spatial distribution. This has been shown [116, 117, 118] to produce results comparable to the full hydrodynamical simulations. From simulations it is found that the relation between temperature and density is well-approximated by a power law:

$$T = T_0(\rho_b/\bar{\rho_b})^\alpha \tag{2.58}$$

,where T_0 is round the order of 10^4 K. We can get the optical depth τ by applying the *fluctuating Gunn-Peterson approximation*:

$$\tau \propto \rho_b^2 T^{-0.7} = A(\rho_b/\bar{\rho_b})^\beta = A(\rho_{DM}/\rho_{\bar{DM}})^\beta \tag{2.59}$$

where,

$$A = 0.946\Big(\frac{1+z}{4}\Big)^{6}\Big(\frac{\Omega_b h^2}{0.0125}\Big)^{2}\Big(\frac{T_0}{10^4 K}\Big)^{-0.7}\Big(\frac{\Gamma}{10^{-12}s^{-1}}\Big)^{-1}\Big(\frac{H(z)}{100kms^{-1}Mpc^{-1}}\Big)^{-1} \quad (2.60)$$

, with $\beta \equiv$ 2-0.7α. Here Γ is the photoionization rate and H(z) is the Hubble expansion rate at redshift z. Then flux is calculated by F=exp(-τ)=exp[-A($\rho_{DM}/\bar{\rho_{DM}}$)$^{\beta}$]

The the flux power spectrum $P_F(k)$ and linear matter matter power spectrum $P(k)$ are complicated function of cosmological parameters $(\sigma_8, \Omega_m, h, n)$ and astrophysical parameters that are related to properties of gas. In order to alleviate degeneracies of decaying dark matter model parameters with other parameters and optimize the constraints, we include the CMB measurement from seven year WMAP data in the fit. These parameter limit extraction from combined cosmological data sets can be conveniently performed with a Monte-Carlo Markov Chain (MCMC) technique using the public code `CosmoMC`.

2.3.1 VHS data & SDSS data

2.3.1.1 VHS data The VHS data [41] contains two spectrum data sets: one has 27 QSO spectra from LUQAS ((Large Sample of UVES Quasar Absorption Spectra) by [33] with mean absorption redshift $< z > \sim 2.25$, and the other one from [34] consists of 30 Keck HIRES spectra and 23 Keck LRIS spectra with $< z > \sim 2.72$ between 2.3 $\lesssim$ z $\lesssim$ 3.2. These data are reanalyzed using a large suite of hydrodynamic simulations to estimate the linear dark matter power spectrum on scales 0.003 s/km $\lesssim$ k $\lesssim$ 0.03 s/km, which roughly corresponds to scale 0.3 h/Mpc $\lesssim$ k $\lesssim$ 3 h/Mpc. Each spectrum was observed with high resolution and high signal-to-noise. However, the dataset has a relatively small number of samples, so this statistical error is large. Therefore, it is shown in [41] that the dependence of the bias function between flux and matter power spectrum $b(k,z) \equiv P_F(k,z)/P(k,z)$ on cosmological parameters can be neglected for this data set. Thus we are going to use the derived matter power spectrum directly in this case. SDSS galaxy 3D power spectrum [119] and CMB observation from seven year WMAP experiment [4] are also included in this joint analysis to help to break degeneracies of cosmological parameters.

2.3.1.2 SDSS data The SDSS collaboration [35] had analyzed 3035 quasar spectra with low resolution and low signal-to-noise. They span a wide redshift range of z=2.2-4.2. They have divided the data into 11 equally-spaced redshift bins and 12 measurements of the flux power spectrum at 0.00141 $\lesssim$ k (s/km) $\lesssim$ 0.01778. With low resolution it can't provide measurement on small scale (k $\gtrsim$ 0.02 s/km), but the large sample number significantly reduces the statistical error on large scale and compensate the low signal-to-noise. Therefore we can't ignore the effect of cosmological parameters on the bias function. We choose to work with flux power spectrum directly. This usually requires a large suite of hydrodynamic simulations to do the calibration. We take the advantage of the tight correlations between temperature and density in IGM and run a suite of dark-matter only simulations instead. This should be able to provide a sensible estimation of the constraining power to the decay model that we are interested in. The caveat is that a more robust result will require running full hydrodynamic simulations, and it is out of the scope for this project since our plan is to provide an proof-of-concept study of this method.

Following the approach of [120], we have approximated the flux power spectrum by a first-order Taylor expansion around the fiducial model for the cosmological/astronomical parameters $\mathbf{p}$:

$$P_F(k,z;\mathbf{p}) = P_F(k,z;\mathbf{p^0}) + \sum_i^N \frac{\partial P_F(k,z;p_i)}{\partial p_i}\Big|_{\mathbf{p}=\mathbf{p^0}} (p_i - p_i^0) \tag{2.61}$$

The difference of flux power spectra as a function of cosmological parameters and redshift are derived using simulations. Although this method will become inaccurate when the points are far from the fiducial model and it assumes that the likelihood distribution is well-described by a multivariate Gaussian function, it has been found [120, 121] to be a good approximation for the standard cosmological/astronomical parameters. We then perform a Monte Carlo Markov chain analysis in these parameters space to take into account the uncertainties associated with them. We have the following set of cosmological parameters: H_0, n_s, σ_8, Ω_m, and also our decay model parameter lifetime Γ^{-1} and kick velocity V_{kick}. For astrophysical nuisance parameters we consider eight parameters. For τ_{eff} we have amplitude τ_{eff}^A and slope at z=3 τ_{eff}^S, so that the evolution of optical depth is described as an

power-law: $\tau_{eff} = \tau^A_{eff}(z=3)[(1+z)/4]^{\tau^S_{eff}}$. For γ and T_0, we both treat them as broken power-law at z=3 with one amplitude parameter and two slopes at z < 3 and z > 3.

Following the suggestion by [35], we include the Si III contamination model by by assuming a linear bias correction of the form $P'_F = [(1+a^2)+2acos(vk)]P_F$, with a = $f_{SiIII}/(1-\bar{\mathcal{F}})$, $f_{SiIII} = 0.011$ and $v = 2271$ km/s.

However, for the decay parameters that we intend to explore, they have highly non-Gaussian distribution. We will follow the way of [121] treating the warm dark matter mass and fraction parameters and run a grid of simulations to sample the decay model parameter space. The grid consists of four different values of the lifetime and four kick velocities (Γ^{-1} = 30, 10, 1, 0.1 (Gyr) and V_{kick} = 70, 100, 200, 500 (km/s)), so we perform 16 additional simulations and interpolate between them. The details of the simulations will be described in §2.3.2

2.3.2 Numerical simulations

For our analysis we use simulation run with parallel N-body code GADGET-2 and a modified version by [29]. The modified version consists of a Monte-Carlo simulation at each time step Δt to determine whether a particle should decay with decay probability $P = \Gamma\Delta t$ should decay. If a particle is designated for decay, it will receive a kick speed V_{kick} in a random direction, and it will be flagged to make sure it will not decay again. Each simulation is with box size of $60h^{-1}$ Mpc and 400^3 dark matter particles. The gravitational softening scale is set to 1 h^{-1} kpc in comoving units and the mass per particle is 2.56×10^8 $h^{-1}M_\odot$. As mentioned in §2.3.1.2, we perform a set of 16 simulations, with Γ^{-1} = 30, 10, 1, 0.1 (Gyr) and V_{kick} = 70, 100, 200, 500 (km/s) to sample the decay parameter space. The cosmological reference model corresponds to a "fiducial" ΛCDM universe with parameters, at z=0, Ω_m=0.273, Ω_Λ=0.727, Ω_b=0.044, n_s=0.967, H_0=70.4 $\mathrm{km}s^{-1}Mpc^{-1}$, and σ_8=0.811. It is consistent with the results of WMAP 7-year data [4]. We also run four additional simulations that change H_0, n_s, σ_8, Ω_m to calculate the power spectrum difference for our Taylor expansion methods. All the decay simulations have the same initial condition as the fiducial run starting at z=99. Snapshots are output at regular inter-vals between redshift

z=4.2 and 2.2. The initial conditions are realized using N-GenIC by displacing particles from a Cartesian grid according to Zel'dovich approximation to obtain distributions that agree with density fluctuation power spectrum from [122].

2.4 ADIABATIC CONTRACTION

Baryonic evolution, although it describes only $\sim$ 5% of the universe's energy density, is driven by more complex dynamical processes occurring on different scales, and can modify the dominant dark matter distribution by transforming gravitational potential energy. As baryons cool and fall toward the center of a dark matter halo, their condensation pulls the host material along, increasing the central density of the halo. This response is typically modeled by theories positing adiabatic contraction (AC) in halos.

First considered by Eggen et al. [123] and Zeldovich et al. [85] for various purposes, the standard AC model which describes the dark matter's contraction in response to the change in baryon potential was introduced and numerically tested by Blumenthal et al. [46, henceforth B86]. In order to simplify the equations governing mass distribution, this early model assumed circular particle orbits, angular momentum conservation, and also prevented "shells" of mass from crossing each other. These limitations were alleviated significantly by Gnedin et al. [47, henceforth G04], in which adiabatic contraction dynamics account for orbital eccentricities while adopting an orbit-averaged radius $\bar{r}$ calculated by simulations.

More recent tests of the G04 model have been made on galactic scales [59], and have also compared different applications of baryonic physics at varying mass scales up to the cluster regime [65], while simulations including a full hydrodynamical treatment have been used to check the answers obtained by standard G04-type models [124, 125, 126]. The general findings of these analyses have shown that the G04 paradigm has improved the predictive capacity of adiabatic contraction theory, but that much further calibration is required to reach the precision necessary for a sensitive probe of dark matter distributions. Here, we ascertain the accuracy of advanced AC models in comparison to a suite of cosmological simulations designed to sensitively test the impact of various baryonic effects on dark matter

Table 2.1: Numerical Parameters of Cosmological Simulations

Run	Box size h^{-1} Mpc	N_p	m_{DM} $h^{-1}M_\odot$	m_{gas} h^{-1} kpc	ϵ	z_{end}
D4dm	33.75	216^3	3.176×10^8		6.25	0.00
D4bh	33.75	2×216^3	2.75×10^8	4.24×10^7	6.25	1.00
D4	33.75	2×216^3	2.75×10^8	4.24×10^7	6.25	1.00
D6dm	33.75	486^3	2.79×10^7		2.73	1.00
D6	33.75	2×486^3	2.75×10^7	4.24×10^6	2.73	1.00

structure formation.

2.4.1 Numerical simulations

In our set of simulations, we explore the parameter space characterized by varying mass and force resolution, as well as differing implementations of baryonic physics in order to systematically distinguish the strength of the dark matter density response as a function of these variables. These cosmological simulations are described in detail by Di Matteo et al. [66], in which a ΛCDM cosmological model evolves according to parameters consistent with the WMAP first-year results: Ω_m=0.3, Ω_Λ= 0.7, primordial power spectral index $n = 1$, Hubble parameter $h = 0.7$, and matter power spectrum normalization σ_8=0.9 [127]).

The numerical experiments are performed with a modified version of GADGET-2 [128], in which baryonic evolution is implemented via the Lagrangian smoothed-particle formalism. Radiative cooling and heating processes are computed with a spatially-uniform photoionizing UV background as in Katz et al. [129], while star formation and the associated supernova feedback are modelled by a subresolution treatment of the multiphase interstellar medium [130]. In Table 2.4.1, we note the basic numerical features of each simulation, with our annotations defined as follows: "D4dm", in which dark matter particles are the sole inhabitants of the material universe and interact only gravitationally; "D4", in which baryons are

included and star formation/feedback are calculated; and "D4bh", which is identical to D4 apart from the addition of energetic feedback via active galactic nuclei (AGN) .In the simulations including AGN feedback, the central black holes in each halo are each represented by a collisionless "sink" particle that grows via accretion of surrounding gas or merger with another black hole. We estimate the accretion rate of gas onto a black hole by using the Bondi-Hoyle-Lyttleton parametrization [131, 132, 133], and we further assume that the coupling efficiency between radiated luminosity and surrounding gas is weak, such that only 5% of the feedback energy is dumped immediately into the SPH smoothing kernel at the position of the black hole. The "D6" simulations are direct counterparts of the "D4" experiments, where the two families have the same initial conditions and cosmological box-size (though they differ in particle number and the scale of gravitational force softening), and the hydrodynamical implementations are identical for the boxes including baryons and their evolution. Throughout this paper, we refer to D6 as the high-resolution counterpart of D4bh, and correspondingly D6dm maps to D4dm. In these cosmological samples, we probe a range in halo virial mass $M_{\rm vir}$ roughly bounded by $3 \times 10^{12} h^{-1} M_{\odot} \lesssim M_{\rm vir} \lesssim 5.2 \times 10^{13} h^{-1} M_{\odot}$. The corresponding range in virial radius $r_{\rm vir}$ is $3.6 \times 10^{2} \lesssim r_{\rm vir} \lesssim 9.4 \times 10^{2} h^{-1}$ kpc.

Computational resources limit us to analysis of these cosmological simulations at redshift $z = 1$ (though we note that the D4dm experiment is complete to the present-day), and throughout this paper we refer to quantities measured at that epoch unless otherwise noted. We define a dark matter halo as a sphere with mean internal density $\bar{\rho}_{180}$ equal to 180 times the mean density $\bar{\rho}_{\rm tot}$ of the entire simulated box. In order to compare halo catalogs directly between different simulations, we identify halo counterparts as those lying within $0.8 R_{\rm vir}$ of each other and with mass difference less than 15%.

2.4.2 Tests on adiabatic contraction models

The standard model introduced by B86 is based on several assumptions. If angular momentum is conserved and dark matter halos are spherically-symmetric, B86 posits the following identity involving dark matter mass $M_{\rm DM}$ and baryonic mass M_b:

$$[M_{DM}(r_i) + M_b(r_i)] r_i = [M_{DM}(r_f) + M_b(r_f)] r_f \tag{2.62}$$

where $M(r)$ is the mass enclosed within a shell of initial radius r_i, which after compression has a final radius r_f. Given the additional assumption that mass shells do not cross (*i.e.* $M_{DM}(r_i) = M_{DM}(r_f)$), it is then possible to calculate the final dark matter distribution given only the initial mass profiles for dark matter and baryons (traditionally modelled by simulation) as well as the final baryonic profile.

This model was later substantially improved by Gnedin et al. [47], who noted that the B86 model could no longer adequately describe simulation work that was beginning to probe the scales of interest at halo centers. Accounting for eccentricities in particle orbits, G04 used the orbit-averaged radius

$$\bar{r} = \frac{2}{T_r} \int_{r_p}^{r_a} r \frac{dr}{v_r} \tag{2.63}$$

where T_r and v_r are the radial period and velocity while r_a and r_p are the apocenter and pericenter, respectively. Using this formalism, G04 found that a more well-conserved quantity during the adiabatic contraction is given by the product of the mass within the orbit-averaged radius and the instantaneous shell radius, *i.e.* $M(\bar{r})r$ is a constant. The orbit-averaged radius $\bar{r}$ at a given radial position can be described by a power law function, according to G04, as follows:

$$\bar{x} = Ax^w, x \equiv r/r_{vir} \tag{2.64}$$

with $A \approx 0.85 \pm 0.05$ and $w \approx 0.8 \pm 0.02$. This simple model has since been extended to account for the variance of $\bar{r}$ with halo mass, redshift, and baryonic physics [65], although significant discrepancies have emerged between best-fit values of A and w and those obtained by inspecting the orbital properties controlled by Eq. 2.63 [59]. In our study, we perform similar tests of the AC formalism's predictive capacity as a function of the physical models implemented in typical cosmological simulations.

As is well-known, there are many ways to estimate halo concentrations as needed for various purposes. In the sort of experiment we describe here, the traditional method involves fitting NFW profiles to dark matter density distributions. However, as recently noted by Prada et al. [134], resolution issues as well as this profile-form assumption can affect fitting techniques at small radii such as those with which we are presently concerned. An alternative definition of concentration has been adopted by some past studies [*e.g.*135], involving an estimate based on the ratio between a halo's virial radius and the radius surrounding a

certain fraction of the halo's total mass. Following this concept, we henceforth define this mass-enclosing concentration as follows:

$$c(x) = \frac{r_{vir}}{r_{m(r)/M_{vir}=x}} \tag{2.65}$$

where x is a variable representing the chosen mass ratio. In the next section we will look at the correlation between AC model accuracy and halo properties like mass-enclosing concentration, demonstrating that model predictions are closely related to a select few of these quantities.

3.0 RESULTS

3.1 WEAK LENSING

3.1.1 Effect on weak lensing power spectrum and large-scale structure

For the first class of DDM model, weak lensing power spectra are altered in two respects. First, the power spectra for potential and density fluctuations are altered in a scale-dependent way. At early epochs, when the matter density is higher in the DDM models than in standard ΛCDM, potential and density fluctuations are larger because the epoch of matter-radiation equality occurs earlier. We have verified that our constraints are insensitive to the epoch at which we normalize the matter density. At late times, DDM decays suppress density and potential fluctuations. We show this dependence of potential fluctuations on DDM lifetime in Figure 3.1. Notice that models of unstable dark matter have greater $P_{\Psi-\Phi}(k)$ on scales $k \gtrsim 10^{-2}\ h\ \mathrm{Mpc}^{-1}$ at high redshift, but this power is suppressed on sub-horizon ($k \gtrsim 10^{-3}\ h\ \mathrm{Mpc}^{-1}$) at lower redshifts. The strong scale dependence in potential power spectra at scales of order $k \sim 0.05\ h\ \mathrm{Mpc}^{-1}$ should be present in convergence spectra projected on multipoles $\ell \sim k\ D_A(z=1) \sim 150$ ($z = 1$ is the median redshift of lensed sources in our model surveys). The different redshift dependence of DDM, which results in greater suppression of power with decreasing redshift, compared to neutrino mass-induced power suppression allows the two to be disentangled. We also find that angular diameter distances are modified at levels that are small compared to the relative potential fluctuations shown in Fig. 3.1. As a consequence, we find that DDM constraints are based mainly on the scale-dependent potential fluctuation modifications rather than on the modified distance scale, which is the primary driver of *dark energy* constraints.

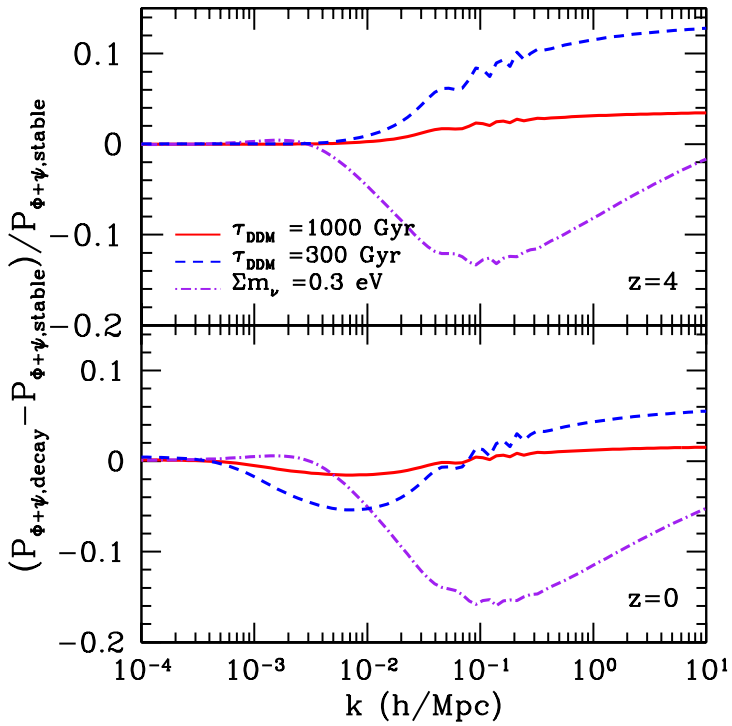

Figure 3.1: Relative difference in the linear potential power spectra between DDM and stable dark matter models at $z = 4$ (*top*) and $z = 0$ (bottom). The *solid* lines show a model with $\tau_{DDM} = \Gamma^{-1} = 10^3$ Gyr while the *dashed* lines have $\Gamma^{-1} = 300$ Gyr. The *dash-dotted* lines show the influence of a non-negligible neutrino mass with $\sum_i \ m_{\nu_i} = 0.3$ eV.

For the second class of DDM, there are several effects of DDM on lensing power spectra at low redshift. First, decays change the cosmological energy density. This change alters both structure growth and distance. However unlike the first class of DDM model, this effect is further suppressed by the mass loss fraction, which is usually a very small number in our study. Further, decaying dark matter results in significant free-streaming of daughter SDM particles. While each of these effects can be important, for models near the limit of what may be constrained by lensing surveys or Lyman-α forest data, it is the effect of free-streaming that largely determines the power spectra. In this case, the free-streaming velocity of SDM suppresses structure growth on scales smaller than free-streaming scale, an effect similar to

that caused by massive neutrinos.

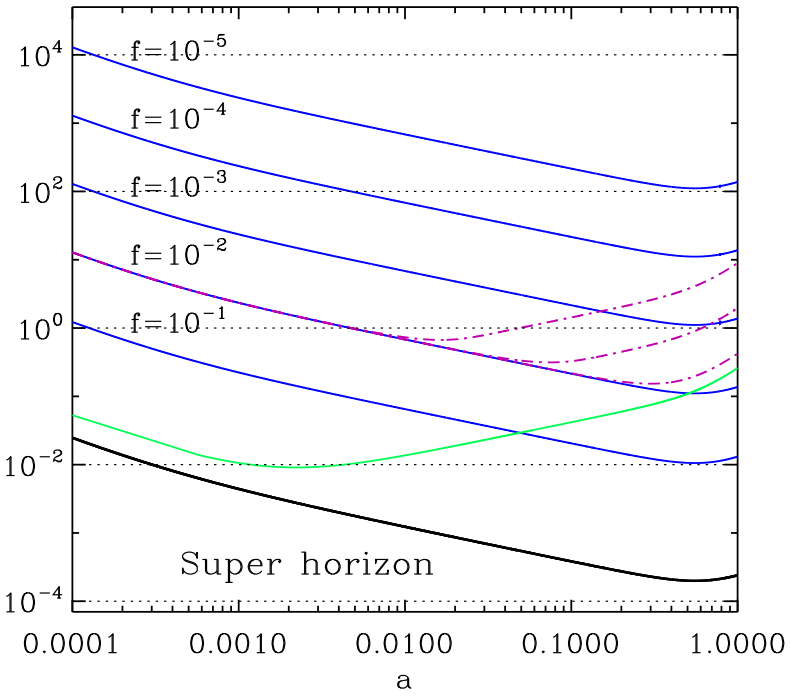

Figure 3.2: Free-streaming scale as a function of scale factor. The blue lines show free-streaming scales for lifetime much greater than the age of universe ($\lesssim$ 100 Gyr) for several different mass loss fractions. The dash-dotted magenta lines are for $f = 10^{-2}$ and three lifetimes. From top-to-bottom at right, these are 0.01 Gyr, 0.1 Gyr, and 1 Gyr. The green line is the free-streaming scale for massive neutrino with $m_{\nu,i}$ =0.4 eV. Structure grows on scales between the free-streaming scale and horizon. On scales smaller than free-streaming scale ($k \lesssim k_{FS}$), structure growth is suppressed.

In the standard cosmological scenario, matter density fluctuations at a particular scale grow once the scale enters the horizon ($k \lesssim H$) during the matter-dominated epoch. However, species with non-negligible primordial velocities will be able to escape the potential wells and suppress the formation of structure. The scale that corresponds to this effect is the free-streaming scale k_{FS}, which can be defined as

$$k_{FS}(a) = \sqrt{\frac{3}{2}} \frac{\mathcal{H}(a)}{c_s(a)}, \tag{3.1}$$

where $\mathcal{H}(a) = a\mathrm{d}a/\mathrm{d}\tau$ and $\mathcal{H}^{-1}$ is the comoving horizon scale.

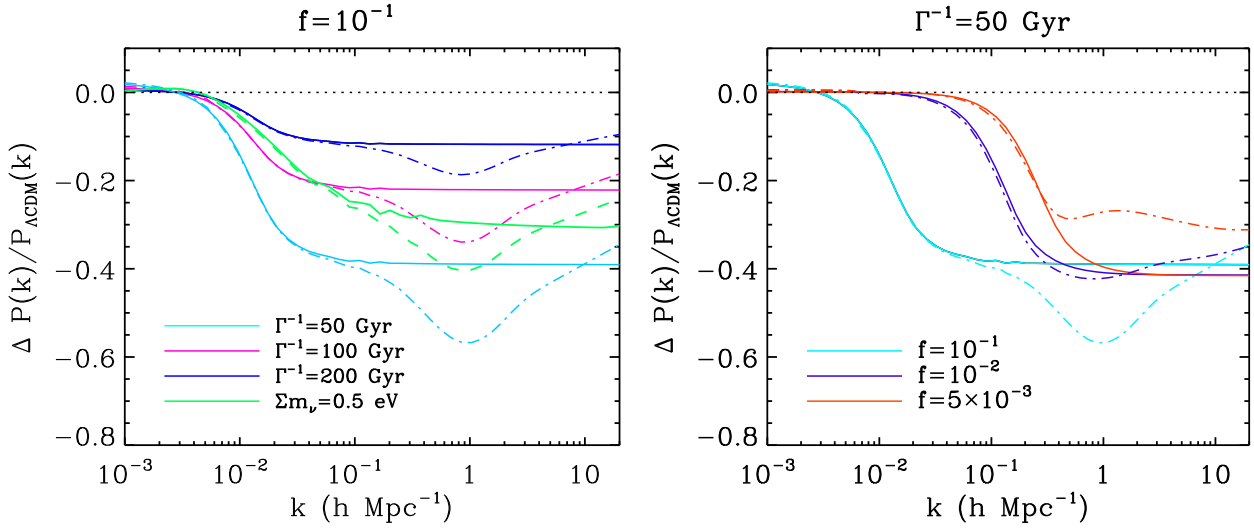

Figure 3.3: Fractional difference between matter power spectrum for standard ΛCDM and a decaying dark matter model evaluated at $z = 0$. *Left*: The effect of varying the DDM lifetime at fixed mass-loss fraction, $f = 10^{-1}$. Solid curves show the linear theory predictions, and dash or dash-dot lines show predictions that include the nonlinear corrections implemented via the halo model. The green lines show the spectrum in a ΛCDM with massive neutrinos, Σm_ν =0.5 eV, for comparison. *Right*: The effect of varying mass-loss fraction f, at a fixed lifetime of $\Gamma^{-1} = 50$ Gyr.

We show the evolution of free-streaming scale of SDM particles as a function of scale factor in Figure 3.2 for several mass loss fractions f and lifetimes. As discussed in [31], the behavior of the free-streaming scale of DDM can be divided into two regimes. When the decay process is still occurring, corresponding to cosmological times less than the decay lifetime, daughter particles with the same physical momentum are continuously created so that the sound speed stays approximately the same. In this case, the evolution of free-streaming scale will simply trace the evolution of horizon. If decays have ceased, which will happen when $\Gamma^{-1} \ll H_0^{-1}$, the sound speed will decrease as $c_s \propto a^{-1}$. The free-streaming scale shrinks as the initial velocities are redshifted away. This effect also happens to massive neutrinos as they become non-relativistic. At early times the neutrino free-streaming scale traces the horizon so long as the neutrinos have relativistic velocities. In Figure 3.2 we

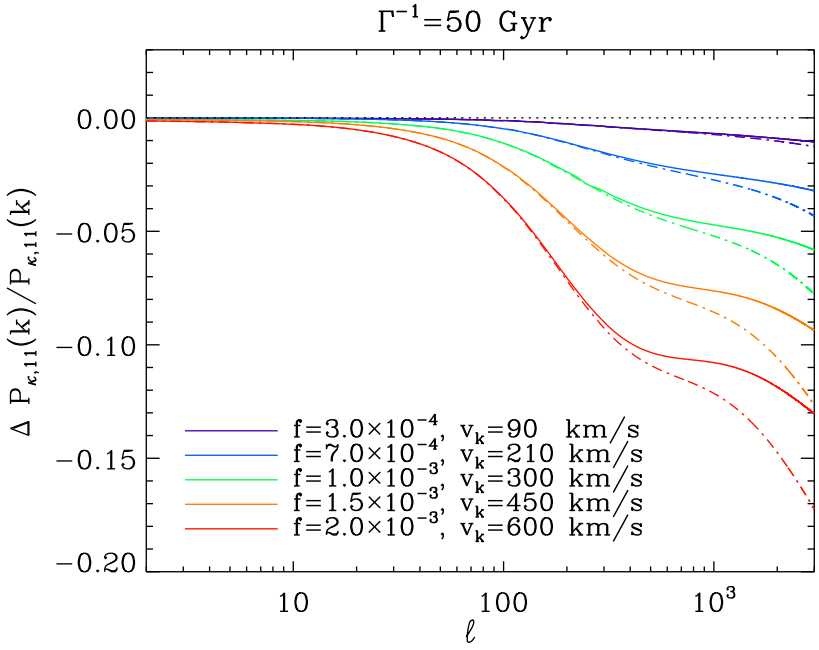

Figure 3.4: Fractional difference of auto convergence lensing power spectrum between standard ΛCDM model and decaying dark matter model from first tomographic redshift bin (lensing source galaxies between $0 < z_p < 0.6$, where z_p is photometric, and not necessarily true redshift). Solid lines are calculated using halo model with NFW profiles. These lines include the alteration of the linear power spectrum on large-scales and the reduction in the abundance of dark matter halos due to free-streaming. However, halos are assumed to have the same profiles as they would in standard ΛCDM. The Dash-dotted lines include the nonlinear corrections to halo density profiles.

can see that after neutrinos become non-relativistic, at $a_{nr} \simeq 1.3 \times 10^{-3}\,(0.4\,\mathrm{eV}/m_\nu)$, their free-streaming scale varies as $k_{FS} \propto a^{1/2}$ during matter domination, which is identical to free-streaming in the small lifetime limit of DDM.

As we mentioned above, DDM affects lensing power spectra in two respects. First, the power spectra for potential and density fluctuations are modified by the free streaming of the daughter SDM particles. At $k \gtrsim k_{FS}$, structure growth is suppressed. Second, the matter

density is reduced as decays occur, slightly suppressing the late-time growth of structure. In the left panel in Figure 3.3, we show that significant decrements in power occur at roughly the same scale, $k \gtrsim 10^{-2} h\,\mathrm{Mpc}^{-1}$ for a variety of lifetimes, so long as the lifetime $\Gamma^{-1} \gg H_0^{-1}$ (the regime most relevant to our work). This suppression is due to free streaming and indeed, the scale on which the suppression occurs agrees with the estimates of the free-streaming scale shown in Fig. 3.2. The right panel of Fig. 3.3 illustrates that the scale of suppression is determined by the mass-loss fraction f, in the limit that $\Gamma^{-1} \gg H_0^{-1}$. In models with larger f, the velocities of the daughter SDM particles are higher, so at fixed lifetime, they free-stream greater distances. Both panels in Fig. 3.3 show a small increment in power on large scales for models with small lifetimes ($\Gamma^{-1} \lesssim 50$ Gyr) and larger mass-loss fractions ($f \gtrsim 0.1$). This delineates the parameter regime for which the overall change in the energy budget begins to have a non-negligible effect on fluctuation growth. The small increment on large scales in these cases enforces a fixed observed CMB normalization.

Notice in the left panel of Fig. 3.3 that with $f \sim 10^{-1}$, the free-streaming suppression is similar to that induced by massive neutrinos with the sum of the neutrino masses $\Sigma m_\nu \approx 0.5$ eV. This suggests that neutrinos may be degenerate with DDM, and this would be the case if it were not possible to probe a wide range of length scales and redshifts. In practice, we find that massive neutrinos are distinguishable from DDM for two reasons. First, the differences in scale dependence exhibited in Fig. 3.3 give a possible handle with which to separate the two. More importantly, the redshift dependence of the power spectrum differs in the two models. This is most easily seen in Fig. 3.2. The evolution of the free-streaming scale of massive neutrinos and the free-streaming scale of DDM differs significantly. Deep, large-scale survey data that enable probes of structure at a variety of redshifts between $0 \lesssim z \lesssim 3$, as is expected of forthcoming surveys, break the potential degeneracy between massive neutrinos and DDM.

The Dash-dotted lines in Figure 3.4 exemplify the alterations to the small-scale lensing convergence power spectra incurred when we account for the altered halo profiles that result from dark matter decays. As f increases, kick velocities increase, and the fractional power decrement increases, as we should expect. This additional suppression is confined to relatively small scales (large multipoles, $\ell \gtrsim 300$) for most of the parameter space of interest

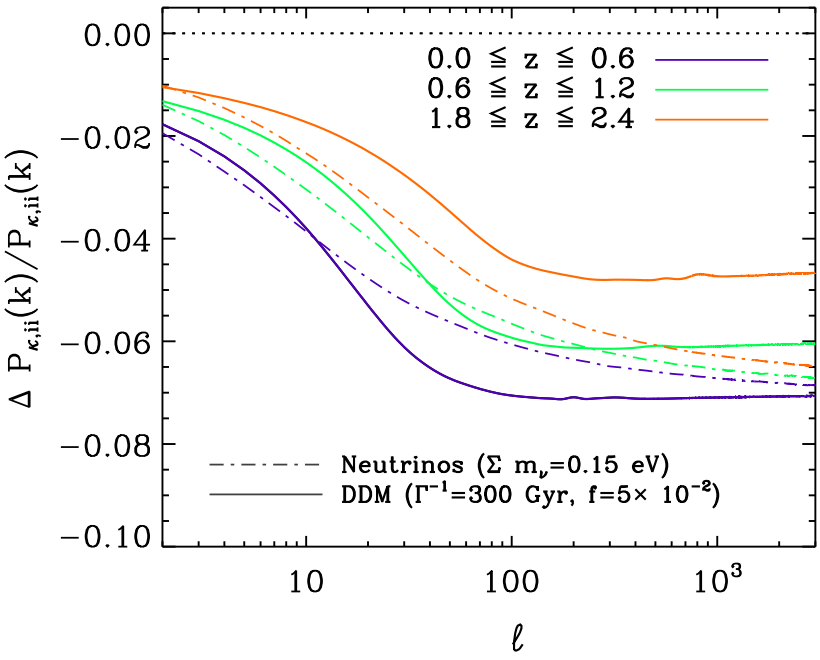

Figure 3.5: Comparison of the redshift evolution of decaying dark matter and massive neutrino lensing power spectra. We plot fractional difference of auto convergence lensing power spectra between standard ΛCDM model and decaying dark matter (or massive neutrino) models in three tomographic redshift bins (labeled at the top). For simplicity, we show only the linear power spectra in this plot, though spectra computed with our nonlinear model lead to a similar conclusion.

($V_k \lesssim$ 200 km/s for $\Gamma^{-1} \lesssim$ 100 Gyr).

As we pointed out in right panel in Figure 3.3, DDM may partially mimic massive neutrinos if redshift evolution information in not accessible. In Figure 3.5, we show a comparison of the redshift evolution of DDM and massive neutrino lensing power spectra in three tomographic redshift bins. Other than the difference in shapes, it is also evident that the DDM power spectra evolve significantly more than the spectra in massive neutrino models. The reason is that the decay process continuously deposits kinetic energy into the daughter dark matter distribution, in contrast to the neutrinos which have purely redshifting kinetic energy

distributions.

3.1.2 Forecasting constraints

To estimate of the power of weak lensing to constrain DDM, we adopt a variety of possible strategies. First, we consider constraints from data on scales where linear evolution of density fluctuations should be valid. The value of this approach is that exploiting linear scales to constrain DDM does not require a simulation program to confirm or refine nonlinear models of structure formation in these models. Moreover, relatively large-scale constraints are less observationally challenging because they exploit data on scales where cosmic variance, rather than galaxy shape measurements, are the dominant error. In both cases, these constraints are conservative so we should expect that forthcoming lensing surveys designed to address dark energy should do *at least as well as our linear forecasts*. To limit ourselves to linear scales, we take data on multipoles $\ell < 300$. All of the constraints that we show in this section have been marginalized over the remaining cosmological parameters, including neutrino mass.

To show the maximum potential of lensing surveys, we consider measurements that extend into the mildly nonlinear regime, as is commonly done for dark energy forecasts. The primary value of this extension is not that particular features in the power spectra induced by DDM are added to the data set. Rather the primary improvement in constraints comes from an increase in the signal-to-noise with which the power suppression can be detected [21, 22]. In this case, we include information on multipoles up to our quoted maximum multipole $\ell_{\rm max} = 3000$ (see § 2.2.1). Constraints on these scales will rely on reliable modeling of clustering on mildly nonlinear scales, so a comprehensive simulation program will be necessary to ensure the robustness of such constraints. A comprehensive program is computationally-intensive and beyond the scope of our studies, as part of our goal is to emphasize that such a large-scale numerical program may be interesting and useful.

We summarize our primary results for the upper limits that may be set on the first class of DDM decay rate Γ, by weak lensing measurements in Table 3.1. The limits in this table have been marginalized over all other cosmological parameters, including neutrino masses. We computed the results in the upper portion of Table 3.1 using contemporary priors on other

Table 3.1: Forecast 68% marginalized limits on the **first class of dark matter model** [21] decay rates from weak lensing surveys under several assumptions. The limits are in units Γ/H_0, where $H_0 = 72$ km/s/Mpc. Constraints are shown for "Linear" power spectra, "Smith et al." nonlinear corrections, "Halo Model" nonlinear corrections, and "Modified Halo Model" nonlinear corrections that account for mass loss as in [80]. The abbreviation "PP" stands for Planck priors.

Experiment	DES	Deep	Wide
Linear, $\ell_{max} = 3000$	0.07	0.06	0.046
Linear, $\ell_{max} = 300$	0.08	0.09	0.057
Smith et al, $\ell_{max} = 3000$	0.03	0.02	0.008
Smith et al, $\ell_{max} = 300$	0.06	0.05	0.029
Halo Model, $\ell_{max} = 3000$,	0.03	0.02	0.010
Modified Halo Model, $\ell_{max} = 3000$,	0.02	0.02	0.008
Linear, $\ell_{max} = 3000$, PP	0.03	0.03	0.016
Linear, $\ell_{max} = 300$, PP	0.06	0.07	0.026
Smith et al, $\ell_{max} = 3000$, PP	0.02	0.01	0.006
Smith et al, $\ell_{max} = 300$, PP	0.05	0.05	0.018
Halo Model, $\ell_{max} = 3000$, PP	0.02	0.02	0.007
Modified Halo Model, $\ell_{max} = 3000$, PP	0.02	0.01	0.006

cosmological parameters. Results below the middle dividing line of Table 3.1 were computed with prior constraints on cosmology at levels expected from the Planck CMB mission and are labeled with a "PP." Different lines in Table 3.1 show results using different model power spectra. The options are the linearly-evolved power spectrum only, results correcting for nonlinear evolution using the Smith et al. [84] formula, nonlinear power results using the halo model, and nonlinear power using the halo model modified to account for the loss of mass within halos (following [80]). In each case, we consider both restricting to linear scales

taking $\ell_{\rm max} = 300$ and using nonlinear information with $\ell_{\rm max} = 3000$ to constrain decaying dark matter.

Constraints that exploit only linear scales are already promising. A DES, a Deep JDEM/WFIRST-like survey, or a Wide LSST- or Euclid-like survey should constrain the DDM lifetime at the level of $\Gamma^{-1} \gtrsim$ 13 H_0^{-1}, $12H_0^{-1}$, and $18H_0^{-1}$ with contemporary priors on other cosmological parameters. These results are already comparable to contemporary, model-independent constraints on unstable dark matter [136, 28, 137, 138, 80, 29] and do not require detailed calibration of nonlinear structure growth or ambitious priors on other cosmological parameters ($\ln \Delta_R^2$ in particular). It seems reasonable then, that weak gravitational lensing will provide, at minimum, a complementary, model-independent technique to constrain DDM that is competitive with other, existing techniques.

If we interpret the other entries in Table 3.1 as possible limits that may be achieved if the necessary nonlinear evolution in models of DDM can be calibrated, then the results become much more interesting. Using contemporary priors, the limits range between $\Gamma^{-1} \gtrsim 33H_0^{-1}$ and $\Gamma^{-1} \gtrsim 43H_0^{-1}$ for DES, $\Gamma^{-1} \gtrsim 48H_0^{-1}$ and $\Gamma^{-1} \gtrsim 66H_0^{-1}$ for our Deep survey, and $\Gamma^{-1} \gtrsim 100H_0^{-1}$ and $\Gamma^{-1} \gtrsim 125H_0^{-1}$ for our Wide survey. The variation between the lower values and higher values exhibits the range of possible constraints estimated using different nonlinear structure formation prescriptions. In all cases, the standard halo model gives the poorest constraint and the halo model modified to account for mass loss as the dark matter decays, as described in § 2.1.2, gives the most stringent constraint. The ability to exploit nonlinear power enables weak lensing to constrain unstable dark matter more stringently than contemporary methods using contemporary priors.

For the second class of DDM model, we display our forecast 1σ exclusion contours alongside a variety of other contemporary constraints In Figure 3.6. The most relevant contemporary constraints come from modifications to the structures of dark matter halos with virial velocities similar to the SDM kick velocities [29] (orange region). Additional constraints may be placed on unstable dark matter by examining the properties of the satellite galaxies of the Milky Way [30] (green regions). However, these constraints rely on a variety of assumptions regarding the formation and evolution of relatively small galaxies. Moreover, these constraints delineate a range of DDM parameters for which unstable dark matter may have

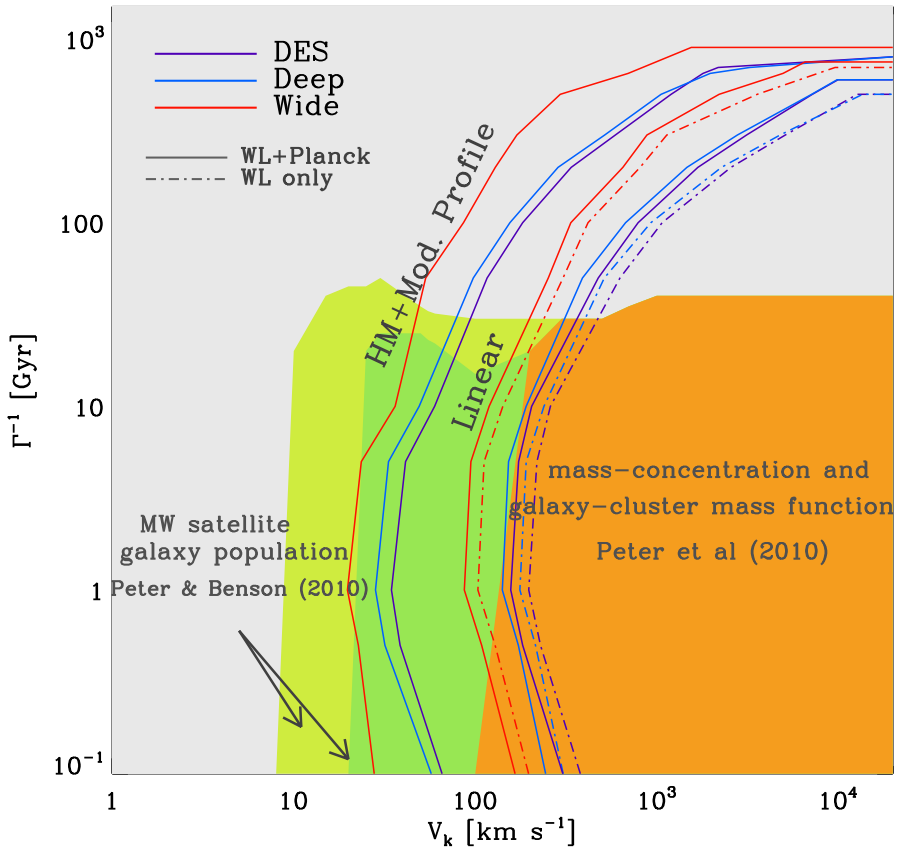

Figure 3.6: Comparison of DDM parameter exclusion contours from Peter et al. [29] (orange) and Peter and Benson [30] (dark and light green) to those that from Lyman-α forest data. The red, purple lines are the 1 σ exclusion contours from our weak lensing forecasts assuming "wide," "deep," and DES like galaxy imaging surveys respectively. The solid lines combine weak lensing with projected Planck constraints, and the dot-dash lines are from weak lensing alone. The less restrictive set of contour lines correspond to constraints using scales on which linear theory is applicable ($\ell < 300$). The more restrictive set of contours incorporate multipoles up to $\ell_{\rm max} = 3000$ and the theoretical calculation includes our nonlinear corrections to halo density profiles.

a significant effect on the interpretation of the missing satellites problem. As this type of DDM model has been invoked to mitigate the "missing satellite" problem, it should not be

a surprise that stronger constraints also come from these types of observations. As such, it is this parameter range for which it is most interesting to develop independent constraints on unstable dark matter and that is the purpose of our weak lensing study.

Again, as indicated in Figure 3.6, our most conservative, linear calculation can already give interesting constraints DDM that are competitive with contemporary bounds. The largest advantage of lensing constraints will be that it can extend constraints on DDM lifetimes significantly, as is evident in Fig. 3.6. These forecasts are not dependent upon modeling nonlinear structure growth, so they constitute a robust lower limit to the constraining power of imaging surveys. Moreover, these constraints are not subject to any particular assumptions regarding the evolution and formation of galaxies, particularly the Milky Way satellite galaxies that are the subject of so much contemporary research. Comparing the linear constraints from the three types of surveys, the "Deep" survey provides slightly more restrictive constraints than DES. A "Wide" survey similar to LSST or Euclid has the potential to improve the constraints relative to DES by ∼40-60%.

The slope of the constraint contours turns over near lifetimes of a few Gyr. This turn over reflects the turn over in free streaming scale exhibited by the dash-dotted lines in Fig. 3.2. In models with $\Gamma^{-1} \ll H_0^{-1}$, the free-streaming scale at low redshift decreases with time. Notice that including Planck priors yields only a marginal improvement on the forecast constraints, $\sim 15 - 40\%$ over the parameter ranges of interest. Our nonlinear forecasts exhibit a similar sensitivity to Planck priors, though they are not depicted in Fig. 3.6 in the interest of clarity.

3.2 LYMAN-α FOREST

3.2.1 Impacts on Lyman-α forest data

As mentioned previously in §2.3.1.1, we will work with the derived-matter power spectrum from the VHS Lyman-α data sets. The effects of DDM model on linear structure growth have been discussed in details in [22]. As discussed in §3.1.1, the free-streaming effect from the excess kick velocity of the decay products suppresses density fluctuation at k$\gtrsim k_{FS}$. The

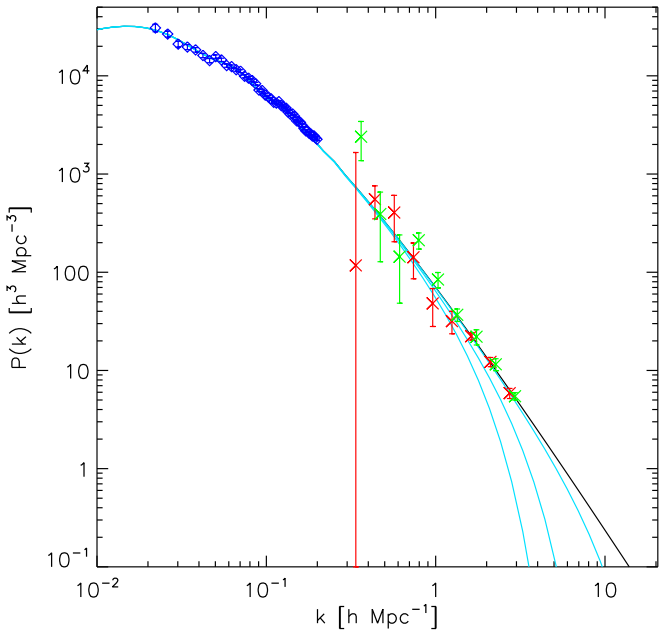

Figure 3.7: Lyman-α-forest-derived matter power spectra from VHS data set and theoretical $P(k)$ for a standard ΛCDM model (solid black) and DDM model [22] with different decay parameter values. Everything has evolved to z=0 for comparison. The blue diamonds are SDSS LRG 3D matter power spectrum [119]. The red points are from Lyman-α forest observation from [34] and green for [33], as re-interpreted by [41]. The cyan lines are DDM suppressed matter power spectrum with Γ^{-1} =1 Gyr and V_k = 30, 100, 150 km/s from top to bottom.

decay lifetime, which determine the abundance of decay daughter particles, will affect the suppression amplitude. These are shown in Fig. 3.3. Here in Fig. 3.7 we show the relevant scale of the data to the DDM suppression of primordial matter spectrum. It is clear from this comparison that Lyman-α forest has the advantage of probing the smallest linear regime, which will provide most of the sensitivities to the small kick velocity regime.

In Fig. 3.8, we plot the Lyman-α forest flux power spectrum versus the SDSS flux power spectrum data from [35] for a few different values of decay parameters. The solid lines are flux spectra derived from standard cold dark matter simulations, and the dash-dotted lines

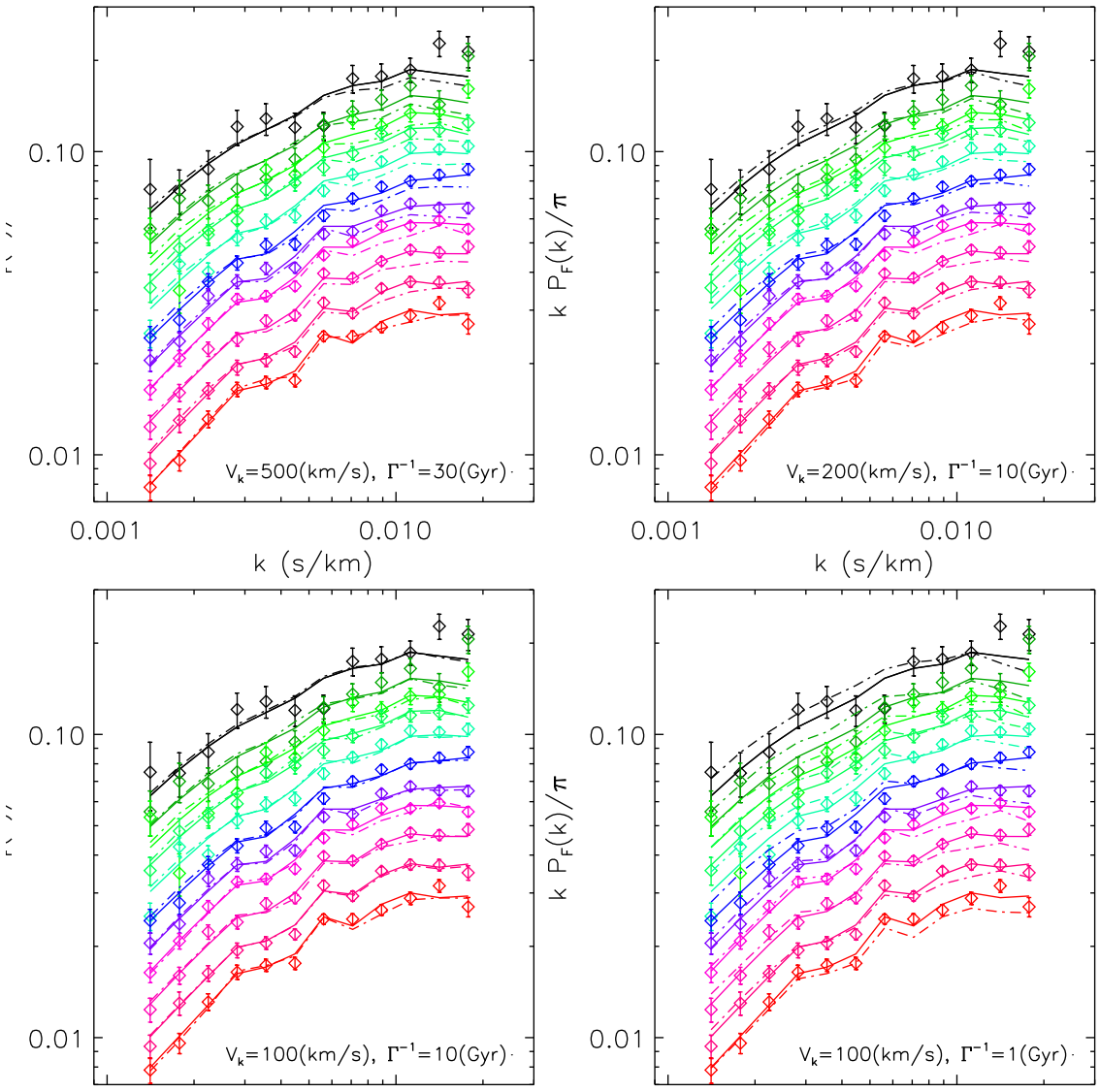

Figure 3.8: Comparison of observed SDSS Lyman-α forest flux power spectra as a function of redshift from z=4.2 (top) to 2.2(bottom) with theoretical model from numerical simulations. For each redshift the solid lines are from the best-fit CDM model, while the dash-dotted lines are for the corresponding DDM model with decay parameter marked in each panel. The response of flux power spectrum to decay parameters are very similar to matter power spectrum, and redshift evolution of the spectrum deviation is greater at late time.

are from simulations with decay modifications. They two types of simulations show good convergence for small kick velocity and large lifetime, as these simulations start from the same initial conditions and decay process changes the properties of some fraction of the dark matter particles as the time evolves. We can see that a similar trend to the matter power spectrum as a function of decay parameters is present. The suppression of power on small scale in DDM make the fit further deviate from the data. The amount of suppression increases from high redshift to low redshift, as from top to bottom in Fig. As time evolves, more decay daughter particles with kick velocity are generated. More significant deviation from the cold dark matter scenario present in low redshift bins. These scale and time-dependence both agree with the behavior we see in matter power spectrum in §3.1.1. Although similar suppression can be induced by massive neutrinos or WDM, the confusion can be easily clear out by their different redshift evolution of the free-streaming effect. This has been discussed in §3.1.1. For either massive neutrino or WDM, they possess extra velocity component (either relativistic or smaller) at they time they are generated at very early time. As the universe expanded, they cool down and the free-streaming scales decrease quickly. Their impacts on both matter and Lyman-α flux power spectrum decrease as time evolves.

3.2.2 Preliminary constraint results

Although not all the intended analysis are done, here we present the preliminary constraint results from the Lyman-α forest data. Here we display our forecast 1σ exclusion contours alongside a variety of other contemporary constraints In Figure 3.9. A direct comparison can be made between Figure 3.9 and Figure 3.6. As we described in §3.1.2, the most relevant contemporary constraints come from modifications to the structures of dark matter halos [29] (orange region). Additional constraints may be acquired by examining the properties of the satellite galaxies of the Milky Way [30] (green regions). From our preliminary results, the Lyman-α-derived matter power spectrum from [41] combining with WMAP 7 data [4] can place constraints slightly better than those using halo structure of galaxy-cluster size halo from [29]. The SDSS flux power spectrum constraints are preliminary and we have not marginalized over cosmological and astrophysical parameters yet. We use simple χ^2

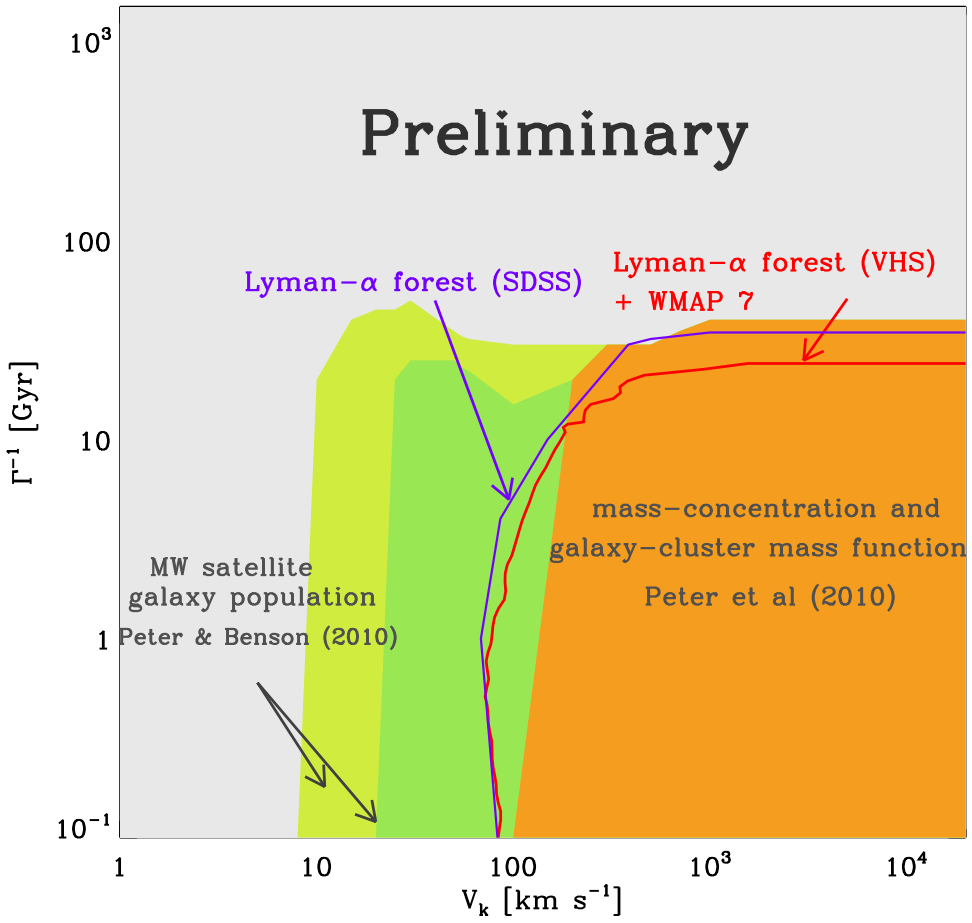

Figure 3.9: Comparison of DDM parameter exclusion contours from [29] (orange) and [30] (dark and light green) to those that are derived from Lyman-α forest data. Notice that the these results are preliminary and we have not marginalized over cosmological and astrophysical parameters in the SDSS constraint. The red line is the 1 σ exclusion contours from VHS data set with WMAP 7 data. The purple line is the 1 σ exclusion contours from SDSS flux power spectrum using the χ^2 deviation for our simulation results.

deviation for our simulation results to estimate the possible 1 σ exclusion contour. For low lifetime, SDSS data is comparable with the VHS data results. Although SDSS flux power spectra have better statistic error, but it extend to slightly lower k value than the VHS

data($k \lesssim 0.02$ s/km comparing to $k \lesssim 0.03$ s/km in VHS data set). The smaller error bars in SDSS data may compensate with the smaller highest k value, and make the constraints from these two data comparable in low lifetime range. However, for lifetime $\Gamma^{-1} \gtrsim 1$ Gyr, the SDSS data starts to provide better constraints that the VHS data. This is likely due to the smaller statistic error of SDSS sample.

3.3 ADIABATIC CONTRACTION

3.3.1 Effects of baryon physics

The baryonic tendency to cool via radiation allows gas to cluster on a smaller scales than that of the corresponding dark matter structure, which can lead to several potentially significant modifications of standard *N*-body cosmological predictions. The exact baryonic distribution at the center of a particular halo is sensitive to and scale-dependent on the physical implementations included in a given simulation. The amount of contraction is also related to the dark matter halo densities, shown in Figure 3.10. The effect of AGN feedback can be seen from the comparison of D4 and D4bh. Central densities in both stars and gas are significantly reduced in D4bh by the presence of AGN feedback, which expels gas from a halo's center and aids the suppression of star formation in that region [while concomitantly enhancing the gas fraction at intermediate radii as shown by 139, in studies of the same simulation suite]. In contrast, the central density of dark matter is higher in the presence of baryons and their associated physics, as theories of adiabatic contraction would predict and hope to model. We note that the D4 simulation, which includes hydrodynamics and star formation but not black hole feedback, is systematically more concentrated in dark matter than the D4bh counterpart, demonstrating that the ejection of gas via AGN can mitigate to some degree the baryon-induced contraction of a halo.

Comparing D4bh and D6, we see that the effects of an increased force/mass resolution are not obvious for objects larger than $10^{13}h^{-1}M_{\odot}$, which correspond to the upper panels of Figure 3.10. For the smaller objects in the lower panels, the baryonic distributions are

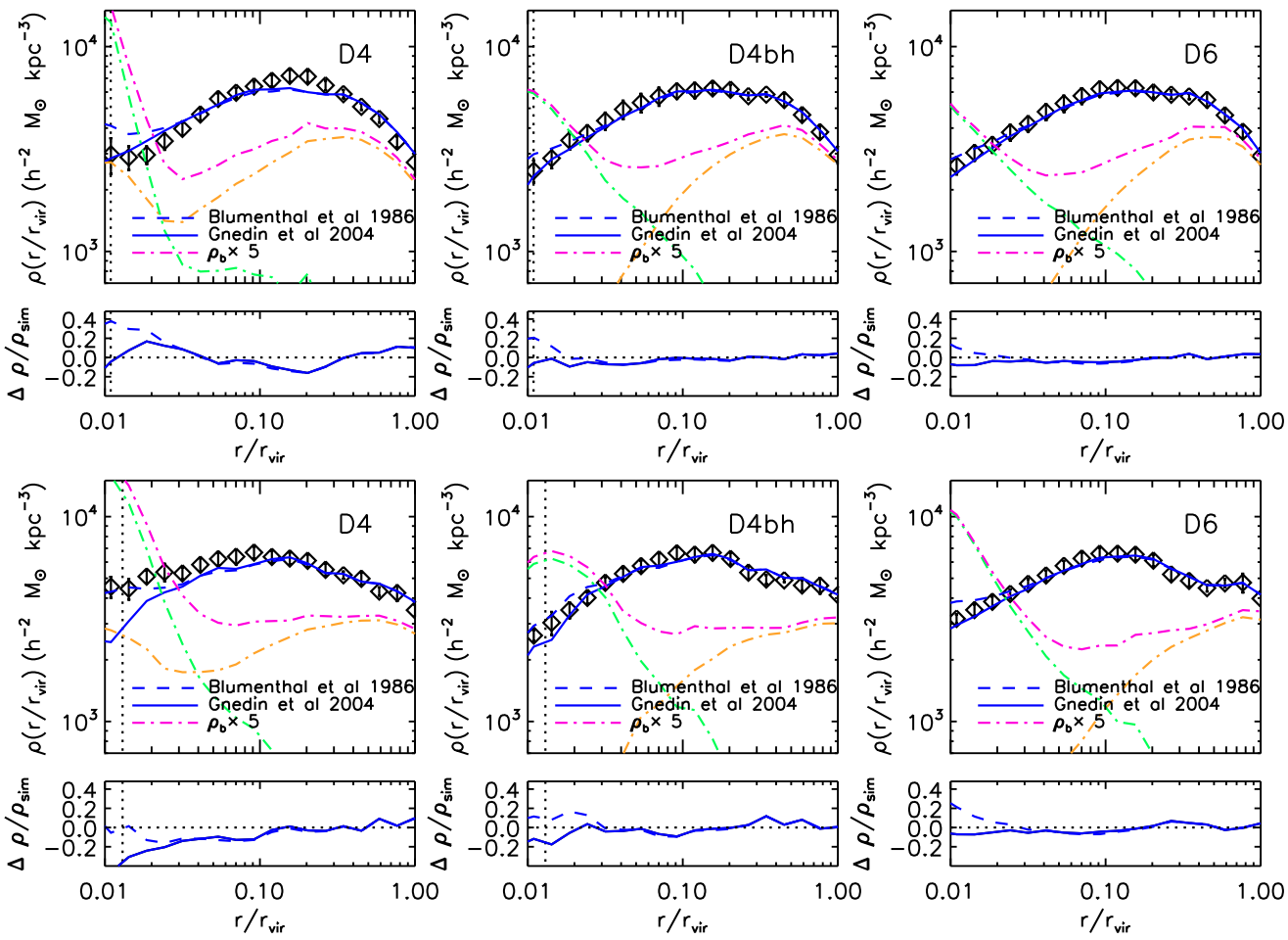

Figure 3.10: Stacked density profiles in the D4, D4bh, and D6 simulations, and the fractional differences between these profiles and the predictions made by two analytic models of adiabatic contraction. We average over 8 halos for two different mass bins: $5.33 \times 10^{13} \lesssim M_{\rm vir} \lesssim 1.20 \times 10^{13} h^{-1} M_\odot$ (*upper* panels), and $5.95 \times 10^{12} \lesssim M_{\rm vir} \lesssim 5.0 \times 10^{12} h^{-1} M_\odot$ (*lower* panels). Black diamonds correspond to dark matter profiles, while *green* and *yellow* dash-dotted lines are stellar and gas density profiles, respectively, and the *pink* dash-dotted line shows the sum of these two baryonic components. The error bars denote the standard deviation of the mean, and all baryonic profiles have been multiplied by 5 for ease of comparison. In each panel, the softening scale is marked by a vertical dotted line representing that scale with respect to the smallest halo in the mass bin.

quite different at higher resolution, since lower-mass halos in D4bh appear to have fewer stars at the center and more gas at intermediate radii than their counterpart objects in D6. This is likely due to the fact that gas density distributions are more well-resolved in D6, thus boosting star formation rates. Although the baryonic matter distributions vary on this level between the two resolution regimes, the behaviors of AC-reconstructed dark matter density profiles in D4bh and D6 agree surprisingly well. The small panels beneath each row in Figure 3.10 show the residuals of each model prediction with respect to the simulated dark matter distributions, and these residuals are quite similar down to a radius $r \sim 0.02 r_{vir}$.

The correlation between central dark matter density and the inclusion of baryonic physics demonstrates conclusively that the distributions of gas and stars in a halo can significantly influence the halo's density profile through the action of gravity alone. Throughout the complex dynamical process of galaxy formation, the subtleties of physics in the ISM as well as the stochasticity of cosmic variance will determine the timescale and degree of a given halo's response, but the basic assumption of AC is clearly robust in the context of standard cosmological experiments. However, generating a mathematical model that recovers the results of adiabatic contraction in halos without the complication of hydrodynamical simulation has proven to be a difficult task, and one which we address in §3.3.2 in order to probe the successes and failures of the standard AC paradigm.

3.3.2 Tests of Adiabatic Contraction Models

In order to test the orbital hypothesis of the G04 model, we examine possible correlations of the power-law parameters A and w with the orbit-averaged radius of Eq. 2.64. Following G04, we calculate the time-averaged radius for dark matter particles in individual halos identified in the D4dm simulation. Approximating halo potentials by spherical NFW profiles drawn from density fitting, we remove unbound particles moving faster than their halo's escape velocity and integrate Eq. 2.63 to obtain the orbit-averaged radius $\bar{r}$ for each particle within the virial radius. In the leftmost panels of Figure 3.11, we bin particles radially between $0.02 \lesssim r/r_{\rm vir} \lesssim 1.0$ and fit the power law of Eq. 2.64, which yields a narrow distribution in the power-law index $0.5 \lesssim w \lesssim 1.0$ that correlates weakly with halo mass. This positive

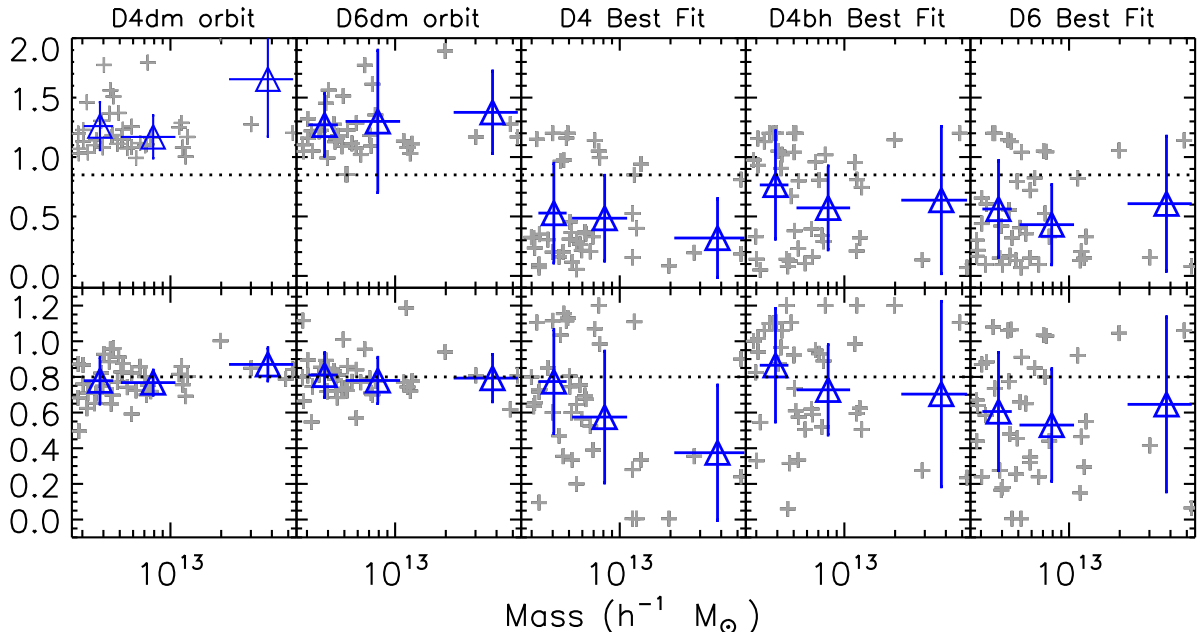

Figure 3.11: Calculated values of A and w in the orbit-averaged radius formalism of G04 (*left* and *center-left* columns, from the D4dm and D6dm dissipationless simulations, respectively), and values fitted by minimizing χ^2 in the hydrodynamical experiments D4, D4bh, and D6 (*center*, *center-right*, and *right* columns respectively), as a function of halo mass. The *dotted horizontal* lines represent the values reported by G04 ($A = 0.85$ and $w = 0.8$). The light crosses denote individual halos and the dark triangles with error-bars represent mean values and variance in each mass bin, as in Figure 3.13.

trend opposes those calculated from the best-fit results in D4 and D4bh hydrodynamical simulations, in which w decreases with halo mass, and the two methods produce distributions in distinctly different regions of parameter space. This suggests that the G04 dynamical model may not be useful for calibrating AC models as applied to individual halos, but that it does reasonably describe the general behavior of dark matter distributions in a statistical sense.

In Figure 3.12, we show the χ^2 distributions of stacked density profiles as a function of varying A and w, over different mass ranges for each set of input baryonic physics. By

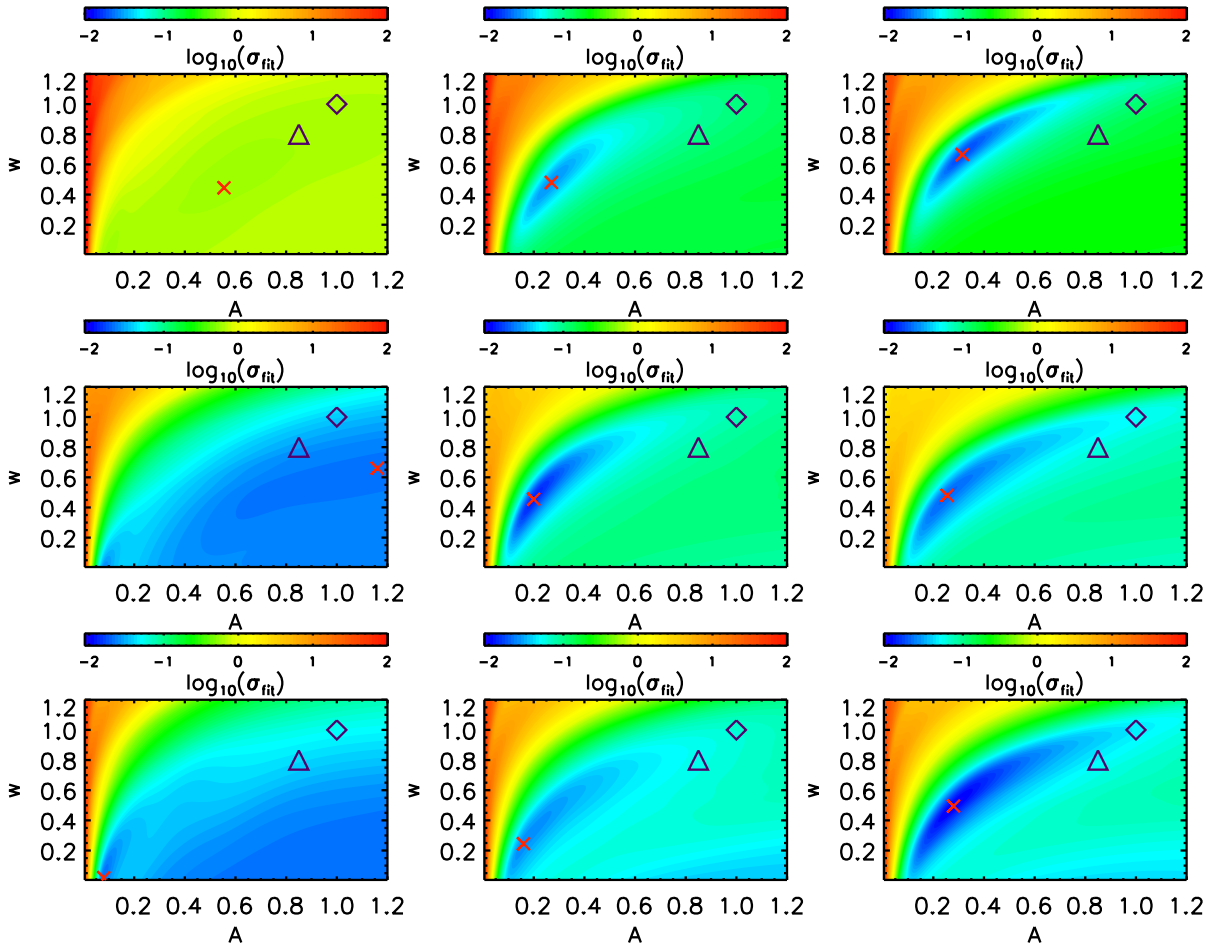

Figure 3.12: Distribution of χ^2 (color-coded from *blue* at minimum values, to *red* at maximum values) according to a fitting of A and w in the orbit-averaged formalism of G04, for stacked dark matter density profiles. Each row represents a cosmological simulation including baryonic physics (D4, D4bh, and D6, from *top* to *bottom*) and the three columns separate the stacked sample into mass bins of $2 - 5.2 \times 10^{13} M_{\odot}$ (*left* panels), $4.4 - 13.0 \times 10^{12} M_{\odot}$ (*center* panels), and $3.0 - 4.3 \times 10^{13}\ h^{-1} M_{\odot}$ (*right* panels). The parameter values found by G04, B86, and our minimum χ^2 fitting are marked by *triangles*, *diamonds*, and *crosses*, respectively. Note that the small number of objects in the leftmost mass bin has significantly widened the contours in χ^2; however, A and w show clear signs of high degeneracy across *all* simulated cosmological boxes.

inspecting these contours from the D4 and D4bh simulations, we note that the presence of AGN feedback in the D4bh run generally results in AC model predictions that are significantly improved matches to the simulated data. Comparing the two resolution regimes, D4bh and D6 show very different behaviors, indicating that numerical effects are affecting our probe of this parameter space. Again, as previous work has shown [59, 65], normalization and power-law index in the G04 formalism are highly degenerate and form extended envelopes of constant χ^2 in the $A - w$ plane. We also note that the best-fit values evolve with halo mass in the D4 simulation, in agreement with the mass-profile residual correlations discussed above.

3.3.3 Correlations with halo properties

The careful calibration of AC models does require an intimate knowledge of how their predictive accuracy correlates with halo parameters derived from simulation. For a variety of properties including (but not limited to) stellar mass fraction, halo mass, and NFW concentration, we check the residual between the mass profiles predicted by adiabatic contraction and those obtained directly through simulation analysis, and in Figure 3.13 we show a selection of interesting correlates appearing at $r = 0.07r_{vir}$. After experimenting with the ratio x in the mass-enclosing concentration defined by Eq. 2.65, we find that a value of $x = 3\%$ (corresponding to a radius $r \sim 0.04 - 0.05$ for most halos) shows obvious correlations in the various simulation experiments. We also show that similar correlations result when NFW concentrations are fitted over the radial range $0.02 - 1.0r_{vir}$, assuming a flat error over this span.

Although the two concentration formalisms have generated similar correlations, only the NFW fitting method probes scales close to the gravitational force-softening length, implying that the mass-enclosing concentration correlations are more robust with respect to numerical resolution. Quantifying this conclusion in Figure 3.14 by calculating the Spearman's-rank coefficient for these correlations, we see obvious positive correlations in the D4 simulation between the mass-profile residual and halo properties drawn from the dissipationless counterpart simulation D4dm, while a negative correlation emerges with respect to the same

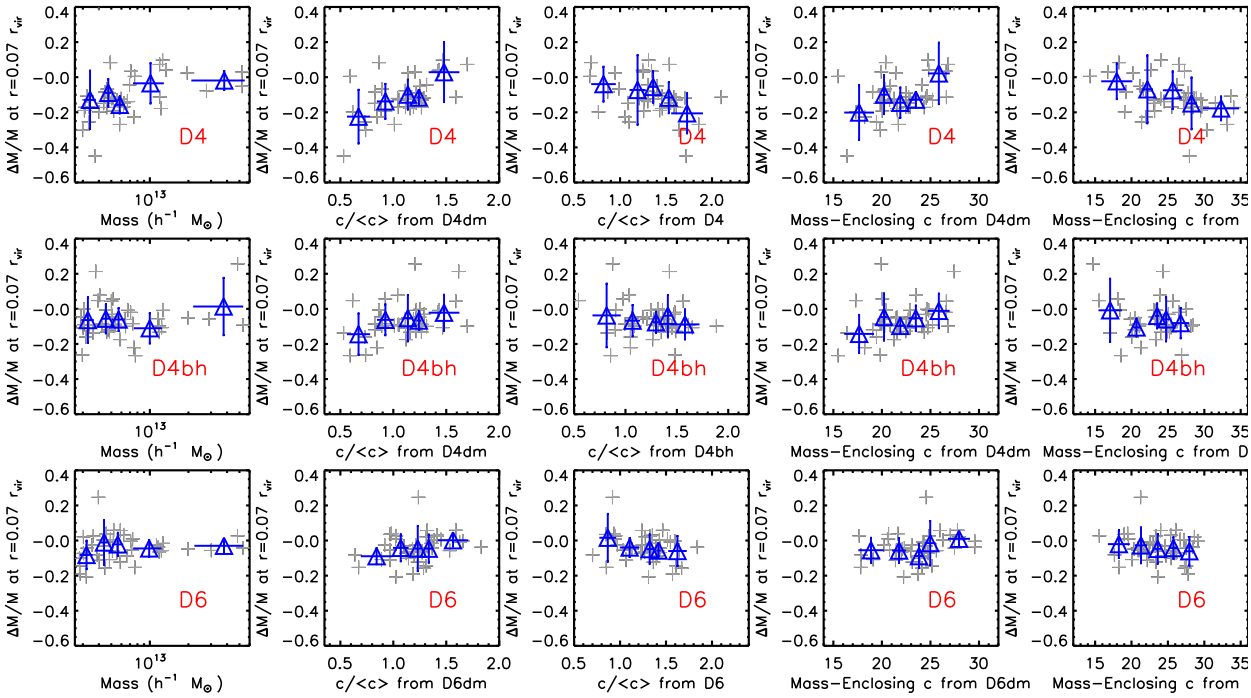

Figure 3.13: Fractional residual in mass enclosed within a radius $r = 0.07r_{vir}$, between the hydrodynamical cosmological experiments and the AC-reconstructed dark matter profiles, as a function of several halo properties drawn from counterpart simulations. Blue triangles and their error-bars represent the mean and variance in mass bins containing the individual halos denoted by crosses. In the second and third columns, we fit concentration values of c according to the NFW formalism for halo profiles outside a minimum radius $r_{min} = 0.02r_{vir}$, while the fourth and fifth columns adopt the mass-enclosing concentration defined by Equation 2.65.

parameters as determined self-consistently from the D4 halo catalog. In contrast, the D4bh simulation (including the baryonic physics of D4 with the addition of AGN feedback) shows a distinct mass-residual correlation only with the concentrations drawn from the D4dm experiment.

In Fig. 3.14, we also attempt to disentangle the NFW concentration parameter from its weak dependence on halo mass, dividing values of c_{180} by the mean concentration value yielded by the model of Macciò et al. [140]. In both hydrodynamical simulations D4 and D4bh, and for both the B86 and G04 models of adiabatic contraction, we find a correlation between prediction residuals and D4dm halo concentrations, at a level exceeding 5% significance for an extended radius out to $r \lesssim 0.1 r_{\rm vir}$. In the panels of Fig. 3.14, we show residuals calculated by the G04 formalism, finding that correlations of similar strength and radial distribution arise for both NFW and mass-enclosing concentration models.

The demonstrated correlations between mass-profile residuals and halo concentration/mass imply that calibrating dark matter distributions with large-scale hydrodynamic simulations can be a significant source of systematic bias in baryonic contraction predictions, favoring certain halo populations over others when semi-analytic galaxy formation models are applied to test the modification of mass profiles. To investigate the strength of this effect in model parameter space, in Figure 3.11 we show the best-fit distributions of the G04 normalization A and power-law index w as a function of halo mass, after tuning the reconstructed density profiles to match those found in the simulations. We estimate the goodness-of-fit for each parameter pair by calculating χ^2 between simulated and AC-predicted values over the radial range $0.025 \lesssim r/r_{\rm vir} \lesssim 1.0$, assuming a flat error in each mass bin. In addition to the wide range in parameter values available, we also note that the trend in w with halo mass is stronger in D4 than in D4bh, reflecting the weaker correlation in the latter simulation between mass-profile residuals and halo mass. At fixed A, an increase in w will boost the amplitude of the density profile near a halo's center, such that the decreasing value of w as a function of halo mass compensates for the growing AC-model residuals at larger masses.

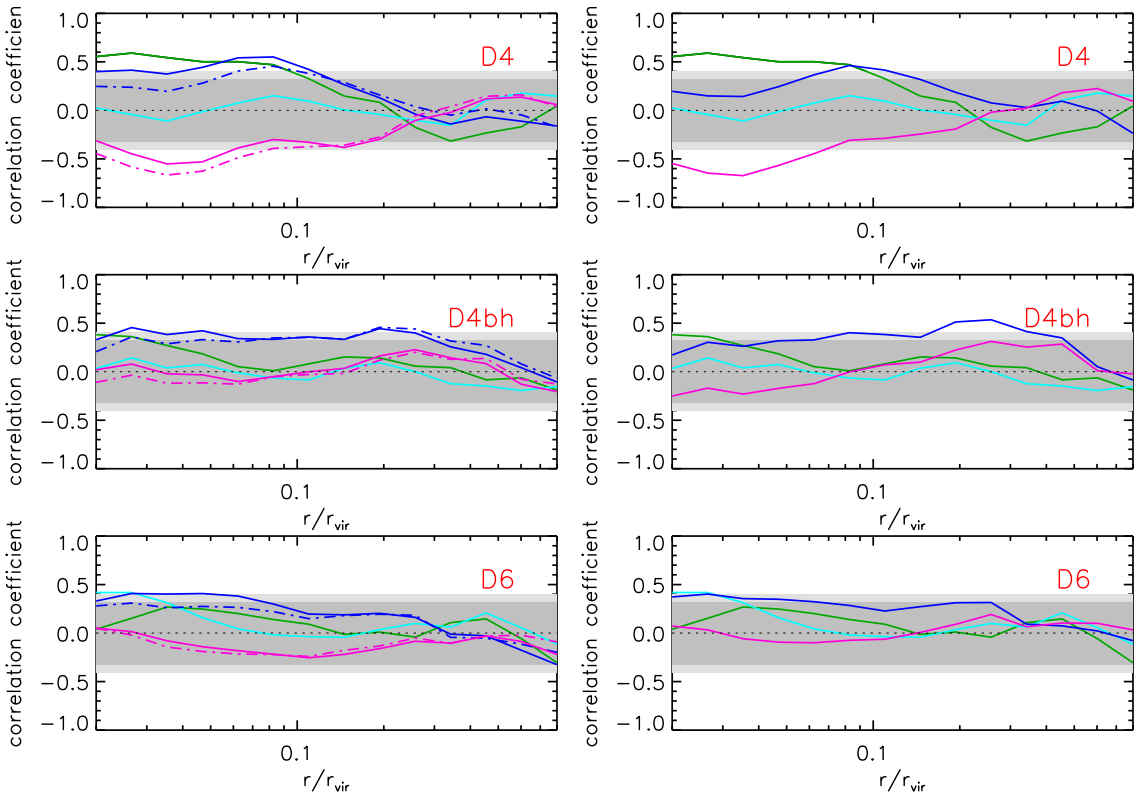

Figure 3.14: Spearman's-rank coefficient of correlations between the fractional mass residuals (for AC-reconstructions by the G04 method and simulated profiles, as presented in Figure 3.13) and several halo properties as a function of radius, for the 40 most massive halos in each hydrodynamical experiment. Larger absolute values of this coefficient imply higher correlations, and the dark (light) shaded region thus encloses the 95% (99%) level of significance; values outside this area indicate that the mass residuals are strongly correlated with a halo property at that radius. *Left* panels use the NFW definition of halo concentration, while *right* panels adopt the mass-enclosing concentration of Eq. 2.65. Solid *green* and *cyan* lines denote halo mass and star fraction, respectively. Solid *blue* and *magenta* lines represent concentration values divided by the mass-dependent mean drawn from Macciò et al. [140], for profiles fit to the dissipationless and hydrodynamical simulations respectively, and the dash-dotted *blue* and *magenta* counterparts represent the original concentration values.

4.0 CONCLUSIONS

In my thesis , I explored a few astrophysical methods for understanding dark matter properties. I investigate the impact of unstable dark matter models on large-scale structure, and also the utility of future or forthcoming weak lensing surveys and contemporary Lyman-α forest data to constrain their properties. For the first class of model that we consider, dark matter decay into light daughter particles. Decaying dark matter can be disentangled from dark energy, because its primary observational signature is to reduce the potential fluctuation power spectrum, while dark energy is primarily constrained by geometric effects [141, 142]. DDM can also be distinguished from massive neutrinos or warm dark matter because the suppression of power is a strong function of redshift. In the second class of model that we consider, DDM decays into a less massive, stable dark matter particle and a significantly lighter particle. The mass difference is parameterized by the velocity kick (V_k) that the daughter, stable dark matter particles receive upon the decay of the heavier, parent DDM. DDM leads to a suppression of matter clustering on scales below the free-streaming scale of the stable, daughter dark matter particles and this suppression can be probed with data from galaxy imaging surveys and Lyman-α forest.

Our most conservative weak lensing constraint forecasts result from considering lensing over large scales on which linear theory should be valid. In this case, best limits which come from a Wide survey, similar to Euclid or LSST. For the first class of DDM model, the forecast limit is $\Gamma^{-1} \lesssim 240$ Gyr , which is stronger than the best contemporary constraints [136, 137, 138, 80]. For the second class of DDM model, these surveys may exclude $V_k \gtrsim 90$ km/s for $\Gamma^{-1} \sim 1 - 5$ Gyr, a result that is competitive with contemporary constraints [29]. For this model, lensing improves upon contemporary constraints most markedly for large decay lifetimes ($\Gamma^{-1} > H_0^{-1}$), which is shown in Figure 3.6. In the relatively near-term, the DES

will be able to place limits of $\Gamma^{-1} \gtrsim$ 160 Gyr for the first class of model and $V_k \gtrsim$ 160 km/s for $\Gamma^{-1} \sim 1 - 5$ Gyr for the second class of model. Achieving constraints at this level should be achievable. First, the lensing surveys we study are under development to study dark energy already. Moreover, these constraints assume that we restrict attention only to relatively large scales on which linear perturbation theory can be used to predict lensing power, so no additional theoretical effort will be necessary.

It may be possible to derive more restrictive lensing constraints on unstable dark matter by considering the mildly nonlinear scales that are commonly considered as part of the program to constrain dark energy. Including multipoles up to $\ell \sim 10^3$ increases constraining power by boosting the signal-to-noise with of the weak lensing signal on scales that are sensitive to the dynamics of the dark matter. Exploiting such scales will rely on an exhaustive simulation program to understand nonlinear clustering in DDM models, similar to the simulation program that is being performed in support of dark energy probes [82], so significant additional theoretical work will be necessary. Nevertheless, the payoff could be significant. In order to estimate the ambitious constraints that may be achieved from such a data analysis, we have implemented nonlinear corrections to lensing power using the standard halo model coupled with a simple model for the modification of halo density structures due to decaying dark matter.

In our most ambitious forecasts, we find that weak lensing may constrain the lifetime or the mass splitting of the DDM nearly an order of magnitude more restrictively than implied by our linear scale analysis. For the first class of DDM, these forecasts are more restrictive than constraints available via other means. For the second class of DDM, it may be possible to achieve similar constraints depending upon a variety of assumptions regarding the formation process of these satellite galaxies [30], but lensing provides a complementary constraint using data on distinct length scales.

We have demonstrated that measurements of the large-scale matter distribution through a weak lensing survey will be a powerful probe of decaying dark matter. This probe is valuable for several reasons. First, such surveys as PanSTARRS, LSST, DES, Euclid, and WFIRST are already being undertaken as part of the effort to constrain dark energy. The survey requirements specified by the dark energy program are the same that we assume

here, so no additional observational work will be necessary. Moreover, we have shown that such measurements can provide independent, competitive constraints on models of DDM that could alter our interpretation of the small-scale problems of the standard cosmological model, particularly the missing satellites problem. In fact, we have demonstrated that lensing will probe DDM models with lifetimes that exceed contemporary bounds by an order of magnitude. Our most ambitious constraint forecasts rely upon the development of accurate and precise models of matter clustering in models of unstable dark matter. This will likely require a significant simulation effort to ensure the robustness of any constraints derived from forthcoming data. It is our hope that this proof-of-concept work will motivate more detailed numerical studies of unstable dark matter models as well as additional possible constraints from related observations.

I also investigate contemporary constraints utilizing Lyman-α data from different measurements [33, 34, 35]. Important extensions of this work will include the complete SDSS data analysis. For the class of DDM that decays into a slightly massive stable daughter particle in which we consider for the Lyman-α study, it shows competitive constraints for both the SDSS data and VHS data regarding the contemporary from [29]. This is exiting because our study using large-scale structure methods can provide promising constraints that will compensate other means using dark halo structures like [29] and [30]. The SDSS data analysis is not completely done. From the preliminary results we can see that the advantage of large sample in SDSS data can provide extra sensitive on large lifetime comparing to VHS data.

On the small scale, we try to understand the effect of baryon on dark matter distribution by study adiabatic contraction models. Testing the assumptions made by AC models of varying complexity requires calibration against dark matter simulations *modulo* input baryonic physics, such that hidden correlations must be identified and thoroughly understood before model predictions can be robustly useful in application. In agreement with previous work, we find that adiabatic contraction theory produces mass profiles that deviate from simulated dark matter distributions to varying degrees in different radial regimes. Calibrating the model parameters of the AC formalism depends on accurately characterizing the underlying correlations with halo properties, since we find that baryonic distributions are linked to halo

concentrations in cosmological simulations both with and without AGN feedback included, strongly implying that the process of contraction plays an important role in molding dark matter density structure on varying scales.

The predictions of adiabatic contraction modelling are much more faithful reproductions of halo density profiles in the hydrodynamical cosmological simulations including black hole physics and associated AGN feedback, likely due to suppression of radiative cooling and subsequent reduction of the baryonic infall rate to a condition much closer to real adiabaticity. The details of feedback energy injection strongly affect this condition, and must be carefully considered when applying AC model predictions to investigations of dark matter structure drawn from baryonic observations (as also noted by [65]). The D4bh simulation is also subject to fewer correlating properties than the D4 run, with mass-profile residuals that only depend on concentrations derived from the dissipationless D4dm counterpart. This allows well-understood N-body results to inform the process of AC model calibration to a much larger degree than in the D4 case without AGN feedback, in which correlations are conflated between halo mass and concentration values calculated in both the hydrodynamical and collisionless contexts. The effects of numerical resolution on the accuracy of AC models are not completely clear, since central density profile parameters in cosmological simulations can be heavily influenced by methodology, as discussed above. However, in the two resolution regimes considered here, the model predictions agree remarkably well for a variety of tested correlates over a wide range in halo mass.

Our analysis shows that adiabatic contraction is a significant factor in the evolution of central density profiles in a ΛCDM universe, and that the implementation of various baryonic physics can strongly affect the accuracy of model predictions compared to cosmological simulations, but it is not well-understood at what level the assumptions made by these models are valid during the complex process of galaxy evolution in the context of hierarchical structure formation. Best-fit constraints on G04 model parameters do not typically recover those values calculated directly by averaging particle orbits, since they evolve differently with halo mass and occupy different regions in $A - w$ space, demonstrating even more concretely that the calibration of any particular adiabatic contraction paradigm is severely limited by our incomplete understanding of galaxy formation and the evolutionary interplay between

baryons and dark matter in cosmological simulations and the real universe.

In summary, in order to understand the nature of dark matter, we must understand both the large- and small-scale phenomena. As many dark matter models are invoked to solve small scale problems, these signals can either be washed out when baryon cools and deepens the potential well, or have significant degeneracy with signatures from strong feedback of supernova or AGN. It is thus essential to understand how baryon physics affect dark matter clustering in halos. Even if we choose to go with large-scale probes, the constraining power usually can be best utilized when we understand the nonlinear modification. No matter which way we go, these two distinct direction will provide constraints that will compensate each other. This is seen as an example in warm dark matter studies. Although WDM has long been the best motivated candidate for understand the small-scale missing satellite and galaxy density profile problems, Lyman-α forest power spectrum has provided the most vigorous constraints so far. The Baryon Oscillation Spectroscopic Survey (BOSS) of SDSS-III will measure Lyman-α forest of 10^5 quasars in the redshift range $2.2 \lesssim$ z $\lesssim 3.5$ and over $\sim 10,000\ deg^2$. The precision of Lyman-α data may soon be greatly improved, and it may provide better evidence to the nature of dark matter. At the same time, as many surveys already have the goal of measuring cosmological weak lensing as a probe of dark energy, similar test on dark matter can be performed largely with the observational infrastructure used to study dark energy at no additional cost. We hope that in the future with the aid of large surveys and theoretical understanding, the mystery of dark matter will soon be solved.

BIBLIOGRAPHY

[1] G. Jungman, M. Kamionkowski, and K. Griest, Phys. Rep. **267**, 195 (1996), arXiv:hep-ph/9506380.

[2] K. Griest and M. Kamionkowski, Phys. Rep. **333**, 167 (2000).

[3] G. Bertone, D. Hooper, and J. Silk, Phys. Rep. **405**, 279 (2005), arXiv:hep-ph/0404175.

[4] E. Komatsu, K. M. Smith, J. Dunkley, C. L. Bennett, B. Gold, G. Hinshaw, N. Jarosik, D. Larson, M. R. Nolta, L. Page, et al., Astrophys. J. Suppl. Ser. **192**, 18 (2011), arXiv:1001.4538.

[5] A. Klypin, A. V. Kravtsov, O. Valenzuela, and F. Prada, Astrophys. J. **522**, 82 (1999), astro-ph/9901240.

[6] B. Moore, S. Ghigna, F. Governato, G. Lake, T. Quinn, J. Stadel, and P. Tozzi, Astrophys. J. Lett. **524**, L19 (1999), arXiv:astro-ph/9907411.

[7] W. J. G. de Blok and A. Bosma, Astron. Astrophys. **385**, 816 (2002), arXiv:astro-ph/0201276.

[8] J. D. Simon, A. D. Bolatto, A. Leroy, L. Blitz, and E. L. Gates, Astrophys. J. **621**, 757 (2005), arXiv:astro-ph/0412035.

[9] R. Kuzio de Naray, S. S. McGaugh, and W. J. G. de Blok, Astrophys. J. **676**, 920 (2008), 0712.0860.

[10] M. Boylan-Kolchin, J. S. Bullock, and M. Kaplinghat, Mon. Not. R. Astron. Soc. **415**, L40 (2011), 1103.0007.

[11] P. Colín, V. Avila-Reese, and O. Valenzuela, Astrophys. J. **542**, 622 (2000), arXiv:astro-ph/0004115.

[12] P. Bode, J. P. Ostriker, and N. Turok, Astrophys. J. **556**, 93 (2001), arXiv:astro-ph/0010389.

[13] A. R. Zentner and J. S. Bullock, Phys. Rev. D **66**, 043003 (2002), arXiv:astro-ph/0205216.

[14] A. R. Zentner and J. S. Bullock, Astrophys. J. **598**, 49 (2003), arXiv:astro-ph/0304292.

[15] M. Lovell, V. Eke, C. Frenk, L. Gao, A. Jenkins, T. Theuns, J. Wang, A. Boyarsky, and O. Ruchayskiy, ArXiv e-prints (2011), arXiv:1104.2929.

[16] D. N. Spergel and P. J. Steinhardt, Physical Review Letters **84**, 3760 (2000), arXiv:astro-ph/9909386.

[17] R. Cen, Astrophys. J. Lett. **546**, L77 (2001), arXiv:astro-ph/0005206.

[18] F. J. Sánchez-Salcedo, The Astrophysical Journal Letters **591**, L107 (2003), arXiv:astro-ph/0305496.

[19] M. Kaplinghat, Phys. Rev. D **72**, 063510 (2005), arXiv:astro-ph/0507300.

[20] A. H. G. Peter, Phys. Rev. D **81**, 083511 (2010), arXiv:1001.3870.

[21] M.-Y. Wang and A. R. Zentner, Phys. Rev. D **82**, 123507 (2010), 1011.2774.

[22] M.-Y. Wang and A. R. Zentner, Phys. Rev. D **85**, 043514 (2012), 1201.2426.

[23] E. D'Onghia and A. Burkert, Astrophys. J. **586**, 12 (2003), arXiv:astro-ph/0206125.

[24] F. Villaescusa-Navarro and N. Dalal, JCAP **3**, 024 (2011), 1010.3008.

[25] A. V. Macciò, S. Paduroiu, D. Anderhalden, A. Schneider, and B. Moore, Mon. Not. R. Astron. Soc. **424**, 1105 (2012), 1202.1282.

[26] M. Rocha, A. H. G. Peter, J. S. Bullock, M. Kaplinghat, S. Garrison-Kimmel, J. Onorbe, and L. A. Moustakas, ArXiv e-prints (2012), 1208.3025.

[27] M. Kaplinghat, R. E. Lopez, S. Dodelson, and R. J. Scherrer, Phys. Rev. D **60**, 123508 (1999), arXiv:astro-ph/9907388.

[28] K. Ichiki, M. Oguri, and K. Takahashi, Physical Review Letters **93**, 071302 (2004), arXiv:astro-ph/0403164.

[29] A. H. G. Peter, C. E. Moody, and M. Kamionkowski, Phys. Rev. D **81**, 103501 (2010), 1003.0419.

[30] A. H. G. Peter and A. J. Benson, Phys. Rev. D **82**, 123521 (2010), 1009.1912.

[31] S. Aoyama, K. Ichiki, D. Nitta, and N. Sugiyama, ArXiv e-prints (2011), arXiv:1106.1984.

[32] V. K. Narayanan, D. N. Spergel, R. Davé, and C.-P. Ma, ArXiv Astrophysics e-prints (2000), arXiv:astro-ph/0005095.

[33] T.-S. Kim, M. Viel, M. G. Haehnelt, R. F. Carswell, and S. Cristiani, Mon. Not. R. Astron. Soc. **347**, 355 (2004), arXiv:astro-ph/0308103.

[34] R. A. C. Croft, D. H. Weinberg, M. Bolte, S. Burles, L. Hernquist, N. Katz, D. Kirkman, and D. Tytler, Astrophys. J. **581**, 20 (2002), arXiv:astro-ph/0012324.

[35] P. McDonald, U. Seljak, S. Burles, D. J. Schlegel, D. H. Weinberg, R. Cen, D. Shih, J. Schaye, D. P. Schneider, N. A. Bahcall, et al., Astrophys. J. Suppl. Ser. **163**, 80 (2006), arXiv:astro-ph/0405013.

[36] M. Viel, J. Lesgourgues, M. G. Haehnelt, S. Matarrese, and A. Riotto, Phys. Rev. D **71**, 063534 (2005), arXiv:astro-ph/0501562.

[37] U. Seljak, A. Makarov, P. McDonald, and H. Trac, Physical Review Letters **97**, 191303 (2006), arXiv:astro-ph/0602430.

[38] F. Governato, C. Brook, L. Mayer, A. Brooks, G. Rhee, J. Wadsley, P. Jonsson, B. Willman, G. Stinson, T. Quinn, et al., Nature **463**, 203 (2010), 0911.2237.

[39] A. V. Macciò, G. Stinson, C. B. Brook, J. Wadsley, H. M. P. Couchman, S. Shen, B. K. Gibson, and T. Quinn, Astrophys. J. Lett. **744**, L9 (2012), 1111.5620.

[40] A. V. Macciò, O. Ruchayskiy, A. Boyarsky, and J. C. Munoz-Cuartas, ArXiv e-prints (2012), 1202.2858.

[41] M. Viel, M. G. Haehnelt, and V. Springel, Mon. Not. R. Astron. Soc. **354**, 684 (2004), arXiv:astro-ph/0404600.

[42] K. Markovic, S. Bridle, A. Slosar, and J. Weller, JCAP **1**, 22 (2011), arXiv:1009.0218.

[43] A. Schneider, R. E. Smith, A. V. Macciò, and B. Moore, Mon. Not. R. Astron. Soc. **424**, 684 (2012), 1112.0330.

[44] M. Viel, K. Markovič, M. Baldi, and J. Weller, Mon. Not. R. Astron. Soc. **421**, 50 (2012), 1107.4094.

[45] R. M. Dunstan, K. N. Abazajian, E. Polisensky, and M. Ricotti, ArXiv e-prints (2011), 1109.6291.

[46] G. R. Blumenthal, S. M. Faber, R. Flores, and J. R. Primack, Astrophys. J. **301**, 27 (1986).

[47] O. Y. Gnedin, A. V. Kravtsov, A. A. Klypin, and D. Nagai, Astrophys. J. **616**, 16 (2004), astro-ph/0406247.

[48] J. A. Sellwood and S. S. McGaugh, Astrophys. J. **634**, 70 (2005), astro-ph/0507589.

[49] D. H. Rudd, A. R. Zentner, and A. V. Kravtsov, Astrophys. J. **672**, 19 (2008), arXiv:astro-ph/0703741.

[50] E. Semboloni, H. Hoekstra, J. Schaye, M. P. van Daalen, and I. G. McCarthy, Mon. Not. R. Astron. Soc. pp. 1461–+ (2011), arXiv:1105.1075.

[51] M. P. van Daalen, J. Schaye, C. M. Booth, and C. Dalla Vecchia, Mon. Not. R. Astron. Soc. **415**, 3649 (2011), arXiv:1104.1174.

[52] A. A. Dutton, F. C. van den Bosch, A. Dekel, and S. Courteau, Astrophys. J. **654**, 27 (2007), arXiv:astro-ph/0604553.

[53] O. Y. Gnedin, D. H. Weinberg, J. Pizagno, F. Prada, and H.-W. Rix, Astrophys. J. **671**, 1115 (2007), arXiv:astro-ph/0607394.

[54] A. A. Dutton and F. C. van den Bosch, MNRAS **396**, 141 (2009), 0810.4963.

[55] L. Bergström, Reports on Progress in Physics **63**, 793 (2000), arXiv:hep-ph/0002126.

[56] F. Prada, A. Klypin, J. Flix, M. Martínez, and E. Simonneau, Physical Review Letters **93**, 241301 (2004), arXiv:astro-ph/0401512.

[57] E. Athanassoula, F.-S. Ling, and E. Nezri, Phys. Rev. D **72**, 083503 (2005), arXiv:astro-ph/0504631.

[58] Y. Mambrini, C. Muñoz, E. Nezri, and F. Prada, JCAP **1**, 010 (2006), arXiv:hep-ph/0506204.

[59] M. Gustafsson, M. Fairbairn, and J. Sommer-Larsen, Phys. Rev. D **74**, 123522 (2006), arXiv:astro-ph/0608634.

[60] D. D. Xu, S. Mao, J. Wang, V. Springel, L. Gao, S. D. M. White, C. S. Frenk, A. Jenkins, G. Li, and J. F. Navarro, MNRAS **398**, 1235 (2009), 0903.4559.

[61] R. Mandelbaum, G. van de Ven, and C. R. Keeton, MNRAS **398**, 635 (2009), 0808.2497.

[62] M. W. Auger, T. Treu, R. Gavazzi, A. S. Bolton, L. V. E. Koopmans, and P. J. Marshall, Astrophys. J. Lett. **721**, L163 (2010), 1007.2409.

[63] I. G. McCarthy, J. Schaye, T. J. Ponman, R. G. Bower, C. M. Booth, C. Dalla Vecchia, R. A. Crain, V. Springel, T. Theuns, and R. P. C. Wiersma, Mon. Not. R. Astron. Soc. **406**, 822 (2010), 0911.2641.

[64] I. G. McCarthy, J. Schaye, R. G. Bower, T. J. Ponman, C. M. Booth, C. Dalla Vecchia, and V. Springel, Mon. Not. R. Astron. Soc. **412**, 1965 (2011), 1008.4799.

[65] A. R. Duffy, J. Schaye, S. T. Kay, C. Dalla Vecchia, R. A. Battye, and C. M. Booth, MNRAS **405**, 2161 (2010), 1001.3447.

[66] T. Di Matteo, J. Colberg, V. Springel, L. Hernquist, and D. Sijacki, Astrophys. J. **676**, 33 (2008), 0705.2269.

[67] C. Ma and E. Bertschinger, Astrophys. J. **455**, 7 (1995), arXiv:astro-ph/9506072.

[68] U. Seljak and M. Zaldarriaga, Astrophys. J. **469**, 437 (1996), arXiv:astro-ph/9603033.

[69] M. White and W. Hu, Astrophys. J. **537**, 1 (2000).

[70] A. Cooray, W. Hu, and J. Miralda-Escude, Astrophys. J. **535**, L9 (2000), astro-ph/0003205.

[71] M. White, Astroparticle Physics **22**, 211 (2004), astro-ph/0405593.

[72] D. Huterer and M. Takada, Astroparticle Physics **23**, 369 (2005), astro-ph/0412142.

[73] F. Schmidt, Phys. Rev. D **78**, 043002 (2008), 0805.4812.

[74] A. R. Zentner, D. H. Rudd, and W. Hu, Phys. Rev. D **77**, 043507 (2008), arXiv:0709.4029.

[75] G. D. Starkman, N. Kaiser, and R. A. Malaney, Astrophys. J. **434**, 12 (1994), arXiv:astro-ph/9312020.

[76] R. E. Lopez, Ph.D. thesis, THE UNIVERSITY OF CHICAGO (1999).

[77] E. Kolb and M. Turner, *The Early Univrse* (Westview Press, 1994).

[78] C. Ma and E. Bertschinger, Astrophys. J. **455**, 7 (1995), arXiv:astro-ph/9506072.

[79] A. Lewis, A. Challinor, and A. Lasenby, Astrophys. J. **538**, 473 (2000), astro-ph/9911177.

[80] A. H. G. Peter, ArXiv e-prints (2010), arXiv:1001.3870.

[81] A. Albrecht, G. Bernstein, R. Cahn, W. L. Freedman, J. Hewitt, W. Hu, J. Huth, M. Kamionkowski, E. W. Kolb, L. Knox, et al., ArXiv Astrophysics e-prints (2006), astro-ph/0609591.

[82] K. Heitmann, M. White, C. Wagner, S. Habib, and D. Higdon, ArXiv:0812.1052 (2008).

[83] A. Cooray and R. Sheth, Phys. Rep. **372**, 1 (2002).

[84] R. E. Smith, J. A. Peacock, A. Jenkins, S. D. M. White, C. S. Frenk, F. R. Pearce, P. A. Thomas, G. Efstathiou, and H. M. P. Couchman, Mon. Not. R. Astron. Soc. **341**, 1311 (2003), astro-ph/0207664.

[85] Y. Zeldovich, A. A. Klypin, M. Y. Khlopov, and V. M. Chechetkin, Soviet J. Nucl. Phys. **31**, 664 (1980).

[86] R. K. Sheth and G. Tormen, Mon. Not. R. Astron. Soc. **308**, 119 (1999), astro-ph/9901122.

[87] A. R. Zentner, International Journal of Modern Physics D **16**, 763 (2007), arXiv:astro-ph/0611454.

[88] J. F. Navarro, C. S. Frenk, and S. D. M. White, Astrophys. J. **490**, 493 (1997), astro-ph/9611107.

[89] D. Huterer, arXiv:1001.1758 (2010).

[90] Z. Ma, W. Hu, and D. Huterer, Astrophys. J. **636**, 21 (2006), astro-ph/0506614.

[91] A. P. Hearin, A. R. Zentner, Z. Ma, and D. Huterer, Astrophys. J. **720**, 1351 (2010), arXiv:1002.3383.

[92] I. Smail, D. W. Hogg, L. Yan, and J. G. Cohen, Astrophys. J. Lett. **449**, L105+ (1995), arXiv:astro-ph/9506095.

[93] I. Smail, R. S. Ellis, M. J. Fitchett, and A. C. Edge, Mon. Not. R. Astron. Soc. **273**, 277 (1995), arXiv:astro-ph/9402049.

[94] J. A. Newman, Astrophys. J. **684**, 88 (2008), arXiv:0805.1409.

[95] G. Bernstein and D. Huterer, Mon. Not. R. Astron. Soc. **401**, 1399 (2010), arXiv:0902.2782.

[96] R. Massey, J. Rhodes, A. Refregier, J. Albert, D. Bacon, G. Bernstein, R. Ellis, B. Jain, T. McKay, S. Perlmutter, et al., Astron. J. **127**, 3089 (2004), arXiv:astro-ph/0304418.

[97] M. M. Kasliwal, R. Massey, R. S. Ellis, S. Miyazaki, and J. Rhodes, Astrophys. J. **684**, 34 (2008), 0710.3588.

[98] L. S. Collaborations, arXiv:0912.0201 (2009).

[99] A. Cooray and W. Hu, Astrophys. J. **554**, 56 (2001), astro-ph/0012087.

[100] C. Vale and M. White, Apj **592**, 699 (2003).

[101] S. Dodelson, C. Shapiro, and M. White, Phys. Rev. D **73**, 023009 (2006), arXiv:astro-ph/0508296.

[102] E. Semboloni, L. van Waerbeke, C. Heymans, T. Hamana, S. Colombi, M. White, and Y. Mellier, Mon. Not. R. Astron. Soc. **375**, L6 (2007), arXiv:astro-ph/0606648.

[103] G. Jungman, M. Kamionkowski, A. Kosowsky, and D. N. Spergel, Phys. Rev. D **54**, 1332 (1996), arXiv:astro-ph/9512139.

[104] M. Tegmark, A. N. Taylor, and A. F. Heavens, Astrophys. J. **480**, 22 (1997), arXiv:astro-ph/9603021.

[105] U. Seljak, Astrophys. J. **482**, 6 (1997), arXiv:astro-ph/9608131.

[106] W. Hu, Astrophys. J. Lett. **522**, L21 (1999), astro-ph/9904153.

[107] A. Kosowsky, M. Milosavljevic, and R. Jimenez, Phys. Rev. D **66**, 063007 (2002), arXiv:astro-ph/0206014.

[108] T. D. Kitching, A. F. Heavens, L. Verde, P. Serra, and A. Melchiorri, Phys. Rev. D **77**, 103008 (2008), arXiv:0801.4565.

[109] A. H. G. Peter, ArXiv e-prints (2009), arXiv:0910.4765.

[110] W. Hu, D. Huterer, and K. M. Smith, Astrophys. J. Lett. **650**, L13 (2006), arXiv:astro-ph/0607316.

[111] S. Hannestad, H. Tu, and Y. Y. Wong, Journal of Cosmology and Astro-Particle Physics **6**, 25 (2006), arXiv:astro-ph/0603019.

[112] K. Ichiki, M. Takada, and T. Takahashi, Phys. Rev. D **79**, 023520 (2009), arXiv:0810.4921.

[113] S. Bird, M. Viel, and M. G. Haehnelt, ArXiv e-prints (2011), arXiv:1109.4416.

[114] S. Saito, M. Takada, and A. Taruya, Physical Review Letters **100**, 191301 (2008), 0801.0607.

[115] A. Refregier, A. Amara, T. D. Kitching, A. Rassat, R. Scaramella, J. Weller, and f. t. Euclid Imaging Consortium, ArXiv:1001.0061 (2010).

[116] R. A. C. Croft, D. H. Weinberg, N. Katz, and L. Hernquist, Astrophys. J. **495**, 44 (1998), arXiv:astro-ph/9708018.

[117] N. Y. Gnedin and L. Hui, Mon. Not. R. Astron. Soc. **296**, 44 (1998), arXiv:astro-ph/9706219.

[118] A. Meiksin and M. White, Mon. Not. R. Astron. Soc. **324**, 141 (2001), arXiv:astro-ph/0008214.

[119] M. Tegmark, D. J. Eisenstein, M. A. Strauss, and et al., Phys. Rev. D **74**, 123507 (2006), astro-ph/0608632.

[120] M. Viel and M. G. Haehnelt, Mon. Not. R. Astron. Soc. **365**, 231 (2006), arXiv:astro-ph/0508177.

[121] A. Boyarsky, J. Lesgourgues, O. Ruchayskiy, and M. Viel, Journal of Cosmology and Astro-Particle Physics **5**, 12 (2009), arXiv:0812.0010.

[122] D. J. Eisenstein and W. Hu, Astrophys. J. **496**, 605 (1998), arXiv:astro-ph/9709112.

[123] O. J. Eggen, D. Lynden-Bell, and A. R. Sandage, Astrophys. J. **136**, 748 (1962).

[124] P. B. Tissera, S. D. M. White, S. Pedrosa, and C. Scannapieco, MNRAS **406**, 922 (2010), 0911.2316.

[125] M. G. Abadi, J. F. Navarro, M. Fardal, A. Babul, and M. Steinmetz, MNRAS **407**, 435 (2010), 0902.2477.

[126] L. G. Book, A. Brooks, A. H. G. Peter, A. J. Benson, and F. Governato, ArXiv e-prints (2010), 1006.4365.

[127] D. N. Spergel, L. Verde, H. V. Peiris, E. Komatsu, M. R. Nolta, C. L. Bennett, M. Halpern, G. Hinshaw, N. Jarosik, A. Kogut, et al., Astrophys. J. Suppl. Ser. **148**, 175 (2003), arXiv:astro-ph/0302209.

[128] V. Springel, MNRAS **364**, 1105 (2005), arXiv:astro-ph/0505010.

[129] N. Katz, D. H. Weinberg, and L. Hernquist, Astrophys. J. Suppl. Ser. **105**, 19 (1996), arXiv:astro-ph/9509107.

[130] V. Springel and L. Hernquist, MNRAS **339**, 289 (2003), arXiv:astro-ph/0206393.

[131] F. Hoyle and R. A. Lyttleton, in Proceeding of the Cambrdge Philisophical Society **405**, 405 (1939).

[132] H. Bondi and F. Hoyle, MNRAS **104**, 273 (1944).

[133] H. Bondi, MNRAS **112**, 195 (1952).

[134] F. Prada, A. A. Klypin, A. J. Cuesta, J. E. Betancort-Rijo, and J. Primack, ArXiv e-prints (2011), arXiv:1104.5130.

[135] V. Avila-Reese, C. Firmani, A. Klypin, and A. V. Kravtsov, Mon. Not. R. Astron. Soc. **310**, 527 (1999), arXiv:astro-ph/9906260.

[136] A. R. Zentner and T. P. Walker, Phys. Rev. D **65**, 063506 (2002), arXiv:astro-ph/0110533.

[137] Y. Gong and X. Chen, Phys. Rev. D **77**, 023009 (2008), arXiv:0802.2296.

[138] S. De Lope Amigo, W. Cheung, Z. Huang, and S. Ng, ArXiv Astrophysics e-prints (2009), arXiv:0812.4016.

[139] S. Bhattacharya, T. Di Matteo, and A. Kosowsky, MNRAS **389**, 34 (2008), 0710.5574.

[140] A. V. Macciò, A. A. Dutton, and F. C. van den Bosch, MNRAS **391**, 1940 (2008), 0805.1926.

[141] H. Zhan and L. Knox, ArXiv Astrophysics e-prints (2006), arXiv:astro-ph/0611159.

[142] A. P. Hearin and A. R. Zentner, Journal of Cosmology and Astro-Particle Physics **4**, 32 (2009), arXiv:0904.3334.